CZECH TECHNICAL UNIVERSITY IN PRAGUE

Faculty of Nuclear Sciences and Physical Engineering

Department of Physics

Bachelor thesis

Coherent production $\mathrm{J}/\psi \to p\bar{p}$ in Pb–Pb ultra-peripheral collisions

Vendulka Fílová

Supervisor: prof. Jesús Guillermo Contreras Nuño, Ph.D.

Prague, 2016

ČESKÉ VYSOKÉ UČENÍ TECHNICKÉ
V PRAZE
Fakulta Jaderná a Fyzikálně Inženýrská
Katedra Fyziky

Bakalářská práce

Koherentní produkce $\mathrm{J}/\psi \rightarrow p\bar{p}$ v ultra-periferálních srážkách Pb–Pb

Vendulka Fílová

Vedoucí: prof. Jesús Guillermo Contreras Nuño, Ph.D.

Praha, 2016

Prohlášení:

Prohlašuji, že jsem svou bakalářskou práci vypracovala samostatně a použila jsem pouze podklady (literaturu, projekty, software, atd.) uvedené v přiloženém seznamu.

Nemám závažný důvod proti užití tohoto školního díla ve smyslu § 60 Zákona č. 121/2000 Sb., o právu autorském, o právech souvisejících s právem autorským a o změně některých zákonů (autorský zákon).

V Praze dne

Vendulka Fílová

Acknowledgement

I would like to express my special appreciation to my supervisor, prof. Jesús Guillermo Contreras Nuño, Ph.D. Without his patience, encouragement, questioning my statements and constant help both with physics and programming this thesis would not have been possible. My thanks also goes to Mgr. Michal Broz, Ph.D. and Ing. Jaroslav Adam who helped me with physics and programming anytime. I would also like to thank all the academic staff at the department of physics for their enthusiasm and willingness to help. Besides the academic staff, my sincere thanks goes to fellow classmates for their personal and academic support. Last but not least, special thanks goes to my friends and family.

Title:
Coherent production $J/\psi \rightarrow p\bar{p}$ in Pb–Pb ultra-peripheral collisions

Author: Vendulka Fílová

Branch of study: Experimental Nuclear and Particle Physics

Sort of project: Bachelor thesis

Supervisor: prof. Jesús Guillermo Contreras Nuño, Ph.D., Department of Physics, Faculty of Nuclear Sciences and Physical Engineering, Czech Technical University in Prague

---

Abstract:

The decay of a J/ψ produced in ultra-peripheral collisions of lead nuclei at the LHC and decaying into the $p\bar{p}$ channel, has been studied using the STARLIGHT Monte Carlo and a full simulation of the ALICE detector corresponding to the data taking conditions of 2011. This branching ratio is smaller than the ones used in the past, but it promises to have better resolution in mass and transverse momentum for the J/ψ. It is found that indeed it is so. Predictions for the potential number of candidates to be found in real data are given. This is the first study of this decay channel in ALICE for coherently photo-produced J/ψ.

Key words: Heavy quarkonia, J/ψ meson, ulta-peripheral heavy-ion collisions, ALICE detector

Název práce:
Koherentní produkce $J/\psi \to p\bar{p}$ v ultra-periferálních srážkách Pb–Pb

Autor: Vendulka Fílová

Abstrakt:

Rozpad J/ψ vzniklého při ultra- periferálních srážkách jader olova na LHC a rozpad na $p\bar{p}$ pár je studován použitím STARLIGHT Monte Carlo data a simulace detektoru ALICE vyhovujícím podmínkám při nabírání dat z roku 2011. Větvící poměr je menší než ty, co byly použity v minulosti, ale je očekáváno lepší rozlišení pro hmotnost a příčnou hybnost částice J/ψ. Toto očekávání je také potvrzeno. Dále je v práci předpovězen počet kandidátů, které lze najít v reálných datech. Toto je první studie koherentně fotoprodukované částice J/ψ rozpadající se do rozpadového kanálu $p\bar{p}$ na ALICE.

Klíčová slova: Těžká kvarkonia, J/ψ mezon, ultra- periferální těžko-iontové srážky, detektor ALICE

Contents

List of Figures

Chapter 1

Introduction

My work is dedicated the measurement of the coherently produced J/ψ which decays into pair of proton and antiproton in lead-lead ultra-peripheral collisions (UPCs) in ALICE. The reason of this investigation is to get more precise resolution of J/ψ than it was measured before in several experiments. The experiment which I use for final comparison of the resolution is the measurement of J/ψ decaying into lepton pair in lead-lead UPCs in ALICE.

The aim of this work is to assess the possibilities of measuring production of J/ψ decaying into $p\bar{p}$ pair in Pb–Pb UPC using the capabilities of the central detectors in ALICE at the LHC. I will analyse Monte Carlo data generated with STARLIGHT. This type of process has never been measured at the LHC before. Subsequently I will compare the results of my analysis with previous measurements.

For fulfilling these objectives. I will briefly present what kind of particles are known, expressly about the particle J/ψ. Further I will briefly summarise the information related to physics of ultra-peripheral collisions and processes that can be observed during these collisions. Also a description of the ALICE detector must be included. Thereafter I analyse the data and present the results of my work.

The thesis is structured into five main chapters. In first chapter I introduce the J/ψ particle. I talk about classes of particles, mainly about mesons and heavy quarkonia. I summarise the main properties of the J/ψ and two experiments that lead to the discovery of J/ψ are presented.

The next chapter is dedicated to introduction to physics of ultra-peripheral collisions. The important quantities are described. Thereafter I characterised the processes that can occur in UPCs. I put emphasis on describing the photoproduction because this process is dominant for the analysis of my work. One special type of photoproduction is exclusive vector meson production. In the final part of this chapter I analyse the exclusive vector meson production related to the Pb–Pb UPCs producing the J/ψ particle. Important quantities and equations are included.

The third chapter characterises several important experiments measuring the J/ψ. These experiments are from different laboratories and different collisions. I show the main ideas of the experiments, how the experiments were done and I summarise what was measured. I include the results of those measurements so I can compare them with results I get from my analysis.

In the following chapter I sum up the information about ALICE detector. In the first place I introduce CERN (Conseil Européen pour la Recherche Nucléaire) and LHC (A Large Hadron Collider), then the subdetectors are described. I emphasise detectors which are important and used in my analysis of this thesis. I try to outline the use of the detectors in relation to detecting the J/ψ produced in UPCs.

The last chapter is dedicated to the analysis and it is divided into two sections. The first section firstly points on the information about data taking and storing them in ALICE and secondly I present the data which I use for this analysis. I briefly describe how they were generated, what is Monte Carlo and STARLIGHT. I declare the selection criteria and triggers I used for the sample of the data. The second section is about the analysis itself. In the beginning I estimate the efficiency and acceptance of the reconstructed events. Also I estimate the efficiency and acceptance of the particular sub-detectors used. I also study the kinematic distributions of the proton and antiproton pair and of the J/ψ. I study the mass resolution of the J/ψ and I compare it to the mass resolution of J/ψ from previous experiments. I try to assess if the resolution is better or not and if this decay channel could be useful to study J/ψ production in UPCs. Similarly I study the transverse momentum distribution. Last part of the analysis is the estimation of the number of the candidates that can be measured during Run 2 for delivered luminosity. All the results and comparisons are summarised in the very last chapter, the conclusion.

The first four chapters of this work are built on information from literature and scientific articles relating to physics of ultra-peripheral collisions, photoproduction, ALICE detector and measurements of J/ψ in UPCs. The fifth chapter is my own analysis of Monte Carlo data. There I present the main results of this thesis.

Chapter 2

Particle J/ψ

2.1 Standard Model

Table 2.1: Table of elementary particles representing matter and forces. In addition the Standard Model has a scalar boson called the Higgs boson.

FERMIONS	
Leptons	Quarks
ν_e	u (up)
ν_μ	d (down)
ν_τ	c (charm)
e	s(strange)
μ	t (top)
τ	b (beauty)

BOSONS	
Forces	Carrier
Strong	g (gluon)
Weak	W^+, W^-, Z^0
Electromagnetic	γ (Photons)

All matter is made of fundamental particles which are governed by four fundamental forces. How these particles and forces are related is described by the Standard Model (SM) of particle physics. The SM was developed in the early 1970 and since then has become established as a well-tested physics theory.

The elementary constituents of matter occur in two types, such as quarks and leptons. Each group consists of six particles divided in three generations. The first generation consists of the lightest and most stable two particles. The heavier and less stable ones belong to second generation and the heaviest and non-stable particles belong to the third generation.

These particles interact with each other via an exchange of bosons. We define three types of interactions. The strong force is a force which holds two or more quarks together and it is carried by gluons. The sector in standard model which deals with the strong interaction is called Quantum Chromodynamics (QCD). The leptons interact via the electromagnetic force, which it is carried by the photon exchange, by the weak force, characterised by the exchange of vector bosons (W^+, W^- and Z^0). In Tab. 2.1 are classified the elementary particles and carriers of the interactions.

Besides the electric charge, quarks carry a different charge, which is called colour and appear in three states: red, green and blue. Gluons also carry this quantum number, which makes them quantitatively different from the photons, which have no charge.

The consequence of this property is that the coupling constant of QCD increases as the distance between quarks grows. Therefore, for large momentum transfers the coupling constant decreases and we can talk about a property known as asymptotic freedom. Because of the asymptotic freedom quarks cannot be observed freely, they are confined inside mesons and baryons, together called hadrons. Mesons are hadrons composed of a quark-antiquark pair and baryons consist of three quarks of different colours. For instance the proton consists of u, u, d quarks and we would expect that the momentum of the proton would be the sum of the momenta of these quarks.

Experimental data from SLAC [1] showed that quarks carry, on average, only half of the momentum of the proton. The rest of the momentum is carried by gluons. Gluons can produce pairs of quark and antiquark, thus at any time there is a probability that the proton contains extra pairs of $u\bar{u}, d\bar{d}, s\bar{s}$. There is a chance of producing even heavier quark pairs such as $c\bar{c}, b\bar{b}, t\bar{t}$ but it is less probable that the lighter ones. The quarks which give rise to the quantum numbers of the hadron are called valance quarks and the additional $q\bar{q}$ pairs are called sea quarks.

In this work I am particularly interested to study high energy particle collisions, where a virtual photon may couple to the gluons and produce a meson in the final state. Because of the confinement property, quarks can not be studied directly, their properties can be studied from hadrons only. Quark gluon plasma (QGP) is a state of matter in which quarks can freely move and they are confined in a single hadron no more. To create this state of matter hadrons must be tightly packed in a very small volume. The QGP can be occur at a temperature of around 175 MeV and the energy density of 0.7 GeV/fm^3. Such high energy densities can be reached through heavy ion collisions.

The probability to find a certain type of parton (*i.e.*, quarks and gluons) at a specific momentum fraction x and a given momentum transfer Q^2 in a proton is given by the parton distribution function (PDF).

In highly energetic hadron collisions, such as p–p, Pb–Pb, the momentum transfer can be large enough to create mesons in a final state which contain heavier quarks, for example the lowest lying state from a $c\bar{c}$ pair which is called the J/ψ meson.

2.2 Heavy quarkonia

Quarkonium is a bound state of a quark and its own antiquark of the same flavour. The combined pair designates then a flavourless meson. Quarkonia refer to the charmonium ($c\bar{c}$) and bottomonium ($b\bar{b}$). The top quark does not occur as quarkonium, since the top quark decays through the electroweak forces before a bound state can form.

2.3 J/ψ and its discovery

J/ψ is the first state of charmonium. It is a bound state of one charm and one anticharm quark. The both charm and anticharm quarks with the spin $\frac{1}{2}\hbar$ are aligned in the same direction. It means that J/ψ has the spin $\frac{1}{2}\hbar + \frac{1}{2}\hbar = 1\hbar$. Mesons with spin $1\hbar$ are called vector mesons. The J/ψ rest mass is measured to be 3.096916 ± 0.30 Gev/c^2 and it has a decay width of 92.9 ± 2.8 keV. The J/ψ meson is normally measured in the decay channels $\mu^+\mu^-$ or e^+e^-, and in this work I am interested in the decay channel to a $p\bar{p}$

pair. The decay width and the lifetime are related as

$$\Gamma = \frac{\bar{h}}{\tau} \tag{2.1}$$

where the Γ denotes the decay width, the $\bar{h}$ is the reduced Planck constant and τ is the mean lifetime. The Γ of a J/ψ leads to a mean lifetime of $\tau \approx 7.09 \cdot 10^{-21} s$.

The existence of the charm quark was predicted in 1970 [2]. The discovery of J/ψ was announced on November 10 in 1974 by two groups working independently [3, 4]. The groups were led by Samuel C. C. Ting and Burton Richter. Therefore the charm quark was discovered. Both of these groups observed a vector meson with higher mass than that of the vector mesons known, ω, ρ and ϕ vector mesons consisted of lighter quarks. The group led by Samuel C. C. Ting named the observed meson J and the group led by Richter ψ. Thus, the discovered particle was named J/ψ.

2.3.1 Samuel C. C. Ting and BNL

Samuel C. C. Ting was a leader of a group from MIT and National Laboratory (BNL). They studied collisions of protons with a beryllium target and measured the e^+e^- pairs as a product. They used a pair spectrometer which has two arms and it is able to measure quite precisely the mass of the pair. To separate the electrons from hadrons Čerenkov counters were used.

Ting's group during the data taking observed a narrow resonance at 3.1 GeV in the invariant mass spectrum of e^+e^-. This new observed particle was named J by Ting's group.

2.3.2 Burton Richter and SPEAR

Burton Richter lead a research group at Standford laboratory and they studied e^+e^- collisions in the centre-of-mass energy region of 2.5 to 7.5 GeV.

The Burton's group measured the anihilation cross section into hadrons and they observed small deviations of cross section at the centre-of-mass energy about 3. GeV. They scanned the region of centre-of-mass energy 3.1 to 3.3 GeV and they observed a huge resonance. The new particle was named the ψ.

Chapter 3

Ultra - peripheral collisions and photoproduction

3.1 Ultra-Peripheral Collisions

Ultra-Peripheral Collisions (UPCs) are collisions characterised by a large impact parameter. The impact parameter is defined as the perpendicular distance between paths of two colliding particles with radii R_1 and R_2. The impact parameter is required to be larger than the sum of R_1 and R_2. A scheme of a such collisions is shown in Figure 3.1. In the Figure 3.1 one can notice that the shape of the colliding particles looks like a pancake. The particles are boosted a look like a pancake due to the Lorentz contraction in the direction of the movement [5].

Accelerated particles, in our case Pb ions, are surrounded by a boosted electromagnetic field. The intensity of the electromagnetic field is proportional to Z^2, where Z is the charge of the nucleus. In 1924, Enrico Fermi showed that the electromagnetic field of charged particle can be treated as a flux of virtual photons [6]. The intensity of the electromagnetic field can be understood as a number of virtual photons surrounding the nucleus. In UPCs, accelerated ions interact via their cloud of those virtual photons (electromagnetically) only, the hadronic interaction is strongly suppressed. These type of reactions are called photo-processes.

3.2 Photoproduction

When we talk about photoproduction, we talk about photo-processes where some particle is produced. Two types of photoproduction processes can be studied in heavy ion UPCs at the LHC. The photon-photon interactions are reactions in which the radiated photons interact with each other and for example produce a di-lepton pair. However, this kind of process is not studied in this work. The second type is a photonuclear interaction. In this kind of interactions, one photon interacts with one of the nucleus. For example a reaction where only a vector meson is produced in the final state in an otherwise empty detector, which is called exclusive vector meson production. The Feynman diagrams for these photo-processes are shown in Figure 3.2.

The photoproduction of vector mesons can be classified in two categories, coherent and incoherent. Collisions where the radiated photon interacts coherently with the

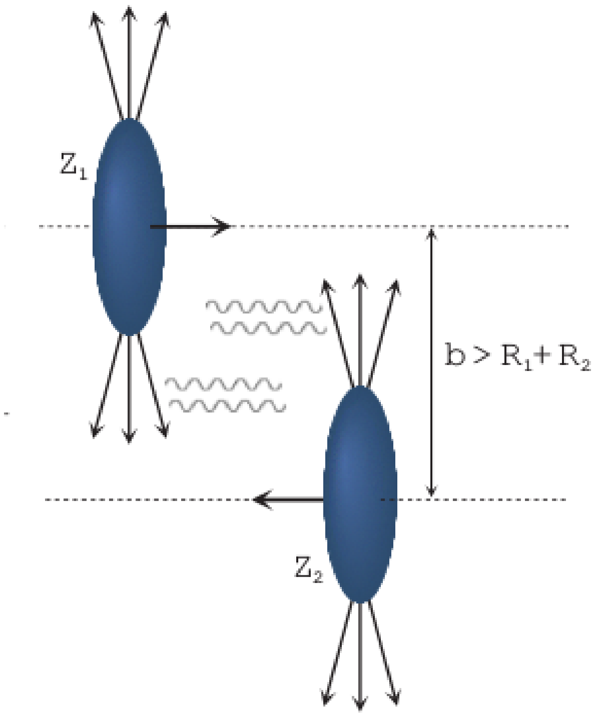

Figure 3.1: A scheme of ultra-peripheral collision, where R_1 and R_2 are radii of colliding particles, b is the impact parameter and Z_1 and Z_2 denote charges of particles.

whole nucleus, we call coherent production. They are characterised by a low transverse momentum of the produced particle which corresponds to a $p_T \backsimeq 60$ MeV/c. It is usual that the nucleus does not break. However, we can occur coherent production with the nuclear break up. Incoherent production are interactions where the photon interacts with a single nucleon. Because the radius of the nucleon is smaller than in case of the whole nucleus, the transverse momentum of the produced system is larger, about $p_T \simeq 500$ MeV/c. The second difference from the coherent production is that the nuclei break up and forward neutrons are produced.

In this work the coherent photoproduction of J/ψ in Pb–Pb UPCs is studied.

3.3 Exclusive vector meson production

Exclusive vector meson production in heavy-ion interactions is used to probe the nuclear gluon distribution, for which there is considerable uncertainty in the low Bjorken-x region. Bjorken-x is a kinematic parameter that represents the fraction of the momentum of the hadron carried by gluons; $x = \frac{p_{gluon}}{p_{hadron}}$. A J/$\psi$ produced at rapidity y is sensitive to the gluon distribution at $x = (\frac{M_{J/\psi}}{\sqrt{s_{NN}}})e^{\pm y}$ at hard scales $Q^2 \approx \frac{M^2_{J/\psi}}{4}$. The total cross section in Pb–Pb interaction can be calculated by the Equation (3.1).

$$\frac{d\sigma_{Pb/Pb}(y)}{dy} = N_{\gamma/Pb}(y,M)\sigma_{\gamma Pb}(y) + N_{\gamma/Pb}(-y,M)\sigma_{\gamma Pb}(-y) \tag{3.1}$$

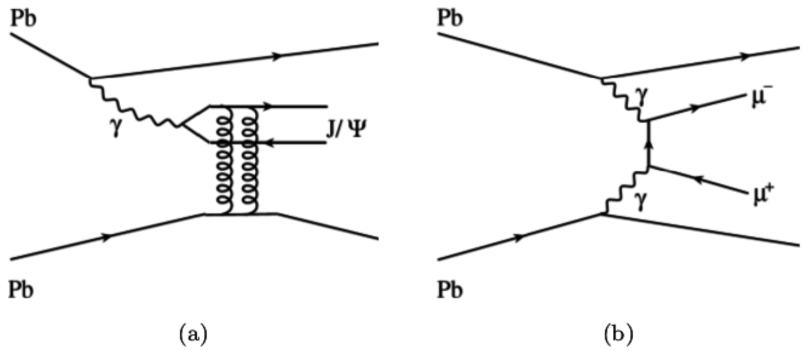

Figure 3.2: Feynman diagrams for (a) the photoproduction of J/ψ, (b) the photon-photon process in Pb–Pb UPCs.

where M is a mass of the produced vector meson state (J/ψ) and y is the rapidity related to k the photon energy through $y = ln(2k/M)$, where $\sigma_{\gamma Pb}(y)$ is the corresponding photoproduction cross section and N_{γ}/Pb is the photon flux. There are two terms because each of the incoming nuclei can act as the photon source. If the photon flux is known, the cross section is a direct measure of the vector meson photoproduction cross section for a given photon energy.

For p–Pb interaction is given a similar formula for the cross section for production of vector mesons. In this case the photon emission by the proton is very small so it can be neglected. The emission by the nucleus is dominant and the total cross section is given by

$$\frac{d\sigma_{Pb/p}(y)}{dy} = N_{\gamma/Pb}(y,M)\sigma_{\gamma p}(y) \tag{3.2}$$

The photon flux is given by a function

$$n(k,b) = \frac{\alpha Z^2}{\pi^2 b^2} x^2 [K_1^2(x) + \frac{1}{\gamma} K_0^2(x)] \tag{3.3}$$

where k is the photon energy in the nucleus frame with Lorentz factor γ, Z is the electric charge of the emitting nuclei, K_0 and K_1 are the Bessel functions and $x = \frac{kb}{\gamma}$. This formula is a good approximation for heavy nuclei in UPC. Then the photon flux is given by

$$n(k) = \frac{2\alpha Z^2}{\pi}[\xi K_0(\xi)K_1(\xi) - \frac{\xi^2}{2}(K_1^2(\xi) - K_0^2(\xi))] \tag{3.4}$$

where $\xi = \frac{kb_{min}}{\gamma}$, b_{min} is the sum of the radii of the interacting particles. The photon flux from a lead nucleus is obtained from

$$N_{\gamma/Pb}(y,M) = k\frac{dn(k)}{dk} \tag{3.5}$$

where the corresponding values of Z, γ and rapidity instead of photon energy are used [7].

There are several models for photonuclear production which are based on Equation 3.1. A model based on the vector dominance model, by Klein and Nystrand [8], is implemented in the STARLIGHT Monte Carlo program and it is used in this work.

Chapter 4

Previous measurements

In this chapter previous relevant measurements of J/ψ are presented.

4.1 ALICE J/ψ measurements in p–Pb and Pb–Pb

At the ALICE detector ultra-peripheral processes producing J/ψ has been measured at mid-rapidity at $\sqrt{s_{NN}} = 2.76$ TeV. In the following are presented results of [9]. In photonuclear interactions the produced vector meson is reconstructed from its decay channels. The exclusively produced J/ψ decays into a lepton pair, where lepton is $\mu^+\mu^-$ or e^+e^-.

This analysis is based on a sample of events collected during the 2011 Pb–Pb data taking. The events were selected with a dedicated barrel ultra-peripheral collision trigger (BUPC), set up to select events with only two tracks in an otherwise empty detector. The analysis was done for both $\mu^+\mu^-$ and e^+e^- decay channels.

The p_T distribution of di-electron (di-muon), integrated over $2.2 < M_{inv} < 3.2$ GeV/c^2, ($3.0 < M_{inv} < 3.2$ GeV/c^2), is shown in Figure 4.1 right (left). The coherent peak at low p_T is clearly visible. The long tail reaching up to 1 GeV is due to incoherent production.

Figure 4.2 shows the invariant mass distribution for $2.2 < M_{inv} < 6.0$ GeV/c^2 for electron and muon pairs. The peak of J/ψ of about 3.1 GeV/c^2 is clearly visible. The tail for lower masses is caused by a radiation of the particles with the detector. Because the interaction probability depends on the mass of the particle traversing the detector for the decay into $p\bar{p}$ pair we expect to get no such striking tail. The J/ψ signal is obtained by fitting a Crystal Ball function. The tail parameters were fixed to those obtained fitting simulated data.

4.2 HERA measurements in ep

The exclusive J/ψ photoproduction, $p + \gamma \rightarrow J/\psi + p$, has been studied in ep collisions at HERA with the ZEUS and H1 detectors. The J/ψ mesons were reconstructed in the leptonic $\mu^+\mu^-$ and e^+e^- decay modes, using the integrated luminosities $L = 38pb^{-1}, L = 55pb^{-1}$.

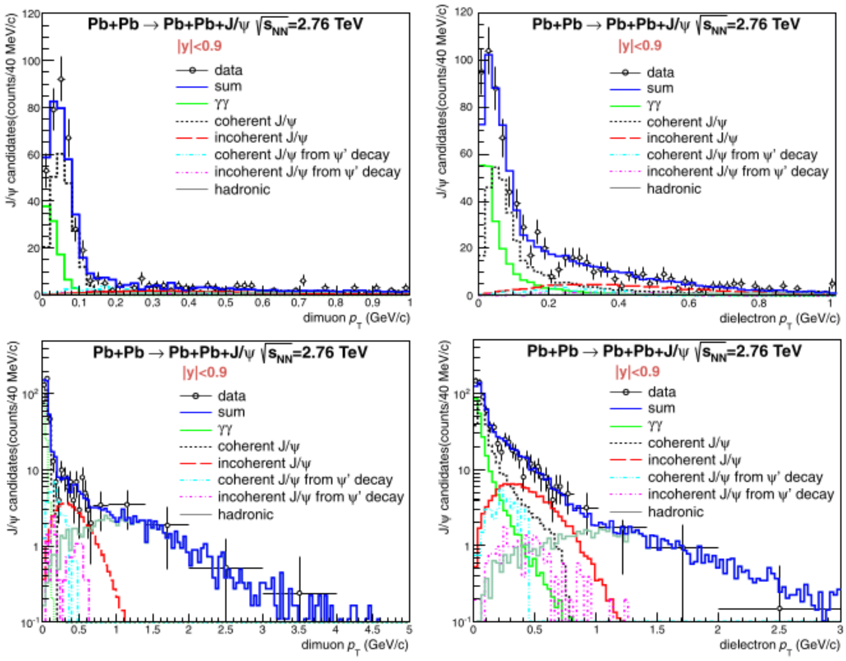

Figure 4.1: $\mu^+\mu^-$ (left) and e^+e^- (right) p_T distribution for Pb–Pb UPCs at $\sqrt{s_{NN}} =$ 2.76TeV for rapidity range $|y| < 0.9$ with the p_T range extended to $p_T < 1$ GeV (top) and to $p_T < 5$ GeV (bottom). Six different functions were used to describe p_T spectrum of coherent J/ψ production (black), incoherent J/ψ production (red), J/ψ from coherent ψ' decay (light blue), J/ψ from incoherent Ψ' decay (purple), $\gamma\gamma$ (green) and J/ψs which were produced in peripheral hadronic interactions (grey). The sum is symbolised by the blue line.

4.2.1 H1 collaboration results

The cross section for elastic production of J/ψ mesons in photoproduction and electroproduction was measured for the photon virtualities Q^2 up to 80 GeV^2 in the range of photon-proton centre-of-mass energy $40 < W_{\gamma p} < 305$ GeV (for the photoproduction) using the integrated luminosity of 55 pb^{-1} [10]. The data used were recorded with H1 detector in years 1999 and 2000. Hera was operated with electron of 27.5 GeV and protons of 920 GeV. The J/ψ mesons were detected via their e^+e^- or $\mu^+\mu^-$ decay channels. The particles were detected in the central and forward tracking detectors.

The cross section for elastic J/ψ production was measured as a function of Q^2 at $W_{\gamma p} = 90$ GeV, see the Figure 4.3. The data from ZEUS are also shown. The cross section was also measured in the dependence on $W_{\gamma p}$. In the Figure 4.4 this dependence is shown for the photoproduced J/ψ mesons.

4.2.2 ZEUS collaboration results

A similar measurement as it was done by H1 detector was done by the ZEUS detector [11]. The exclusively photoproduced J/ψ mesons were measured in their $\mu^+\mu^-$ and e^+e^- decay channels in the kinematic range of photon-proton centre-of-mass energy $20 < W_{\gamma p} < 290$ GeV and for the range of squared four-momentum transfer at the

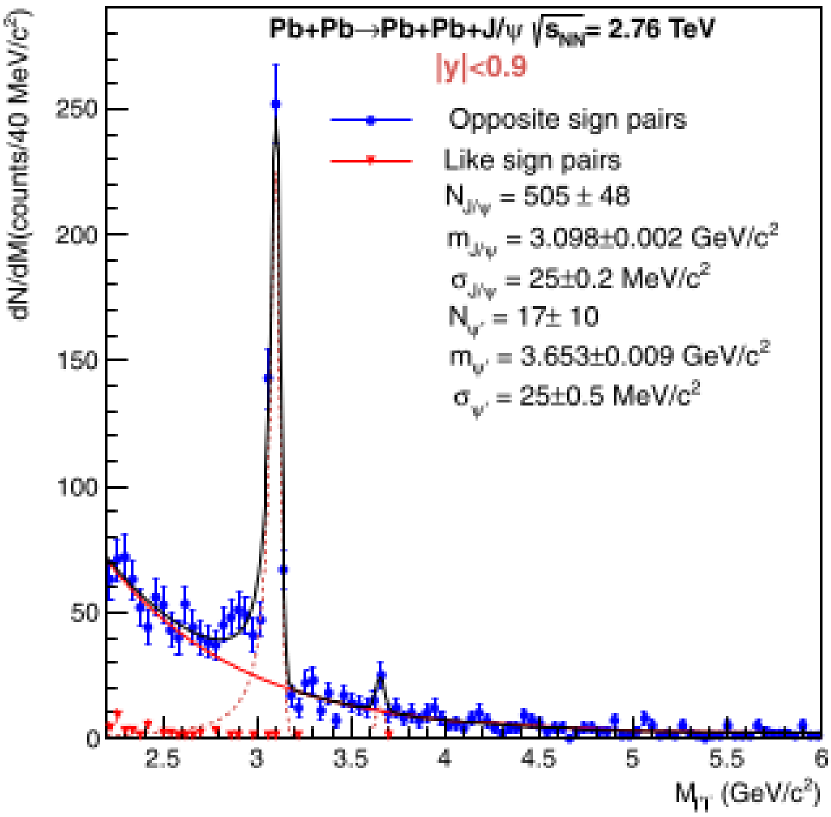

Figure 4.2: The invariant mass distribution for Pb–Pb UPCs at $\sqrt{s_{NN}} = 2.76$ TeV for $-0.9 < y < 0.9$ in the invariant mass interval $2.2 < M_{inv} < 6$ GeV/c^2. Coherent production for $\mu^+\mu^-$ and e^+e^- are summed together. The J/ψ signal is obtained by fitting the opposite sign pairs with the Crystal Ball function.

proton vertex $|t| < 1.8$ GeV^2 using the luminosities 38 pb^{-1} and 55 pb^{-1}.

4.3 Tevatron measurements in $p\bar{p}$

Exclusive J/ψ photoproduction in $p\bar{p}$ collisions has been studied at the Fermilab Tevatron [12]. It was the first measurement of exclusively produced J/ψ meson in hadron-hadron collisions. The $p\bar{p}$ collision data at $\sqrt{s} = 1.96$ TeV with an integrated luminosity $L = 1.48$ fb^{-1} were used. The central exclusive processes, $p + \bar{p} \to p + \mathrm{J}/\psi + \bar{p}$, where $\mathrm{J}/\psi \to \mu^+\mu^-$. The colliding hadrons emerge intact with a small p_T and the exclusively produced J/ψ meson is in the central region and can be fully measured. The were 402 events selected. The $M_{\mu^+\mu^-}$ spectrum is shown in Figure 4.5.

4.3.1 LHCb measurements in pp

The following paragraph is based on results published in [13].

Also in LHCb detector the J/ψ and $\psi(2S)$ exclusively produced vector mesons were observed in di-muon decay channel. The process $p+\gamma \rightarrow \mathrm{J}/\psi + p$ has been measured in the range of pseudorapidity $2 < \eta_{\mu^+\mu^-} < 4.5$ at a proton-proton centre-of-mass energy of $\sqrt{s} = 7$ TeV. The results are consistent with results obtained from HERA and in the Figure 4.6 the total cross sections of the J/ψ photoproduction from LHCb and H1, ZEUS detectors at HERA are shown.

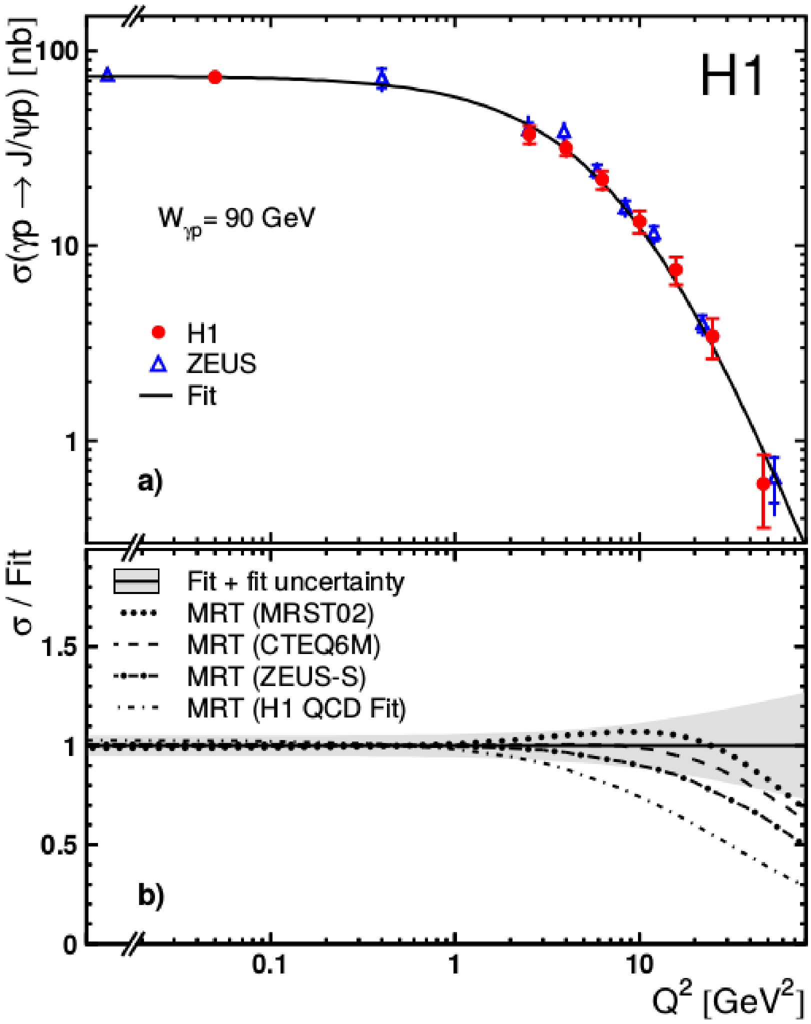

Figure 4.3: The total cross section for elastic J/ψ production as a function of $W_{\gamma p}$ in the range $|t| < 1.2$ GeV^2 for photoproduction. Results from the ZEUS experiment in a similar kinematic range are included.

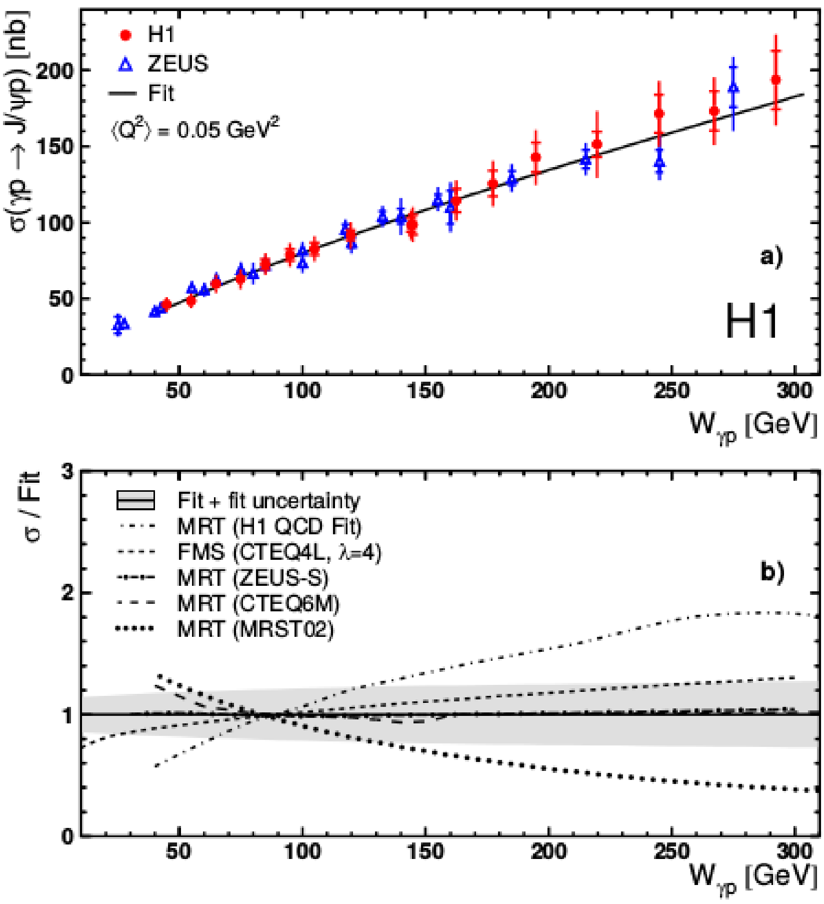

Figure 4.4: The total cross section for elastic J/ψ production as a function of Q^2 at $W_{\gamma p} = 90$ GeV and $|t| < 1.2$ GeV^2. Data from the ZEUS are also shown.

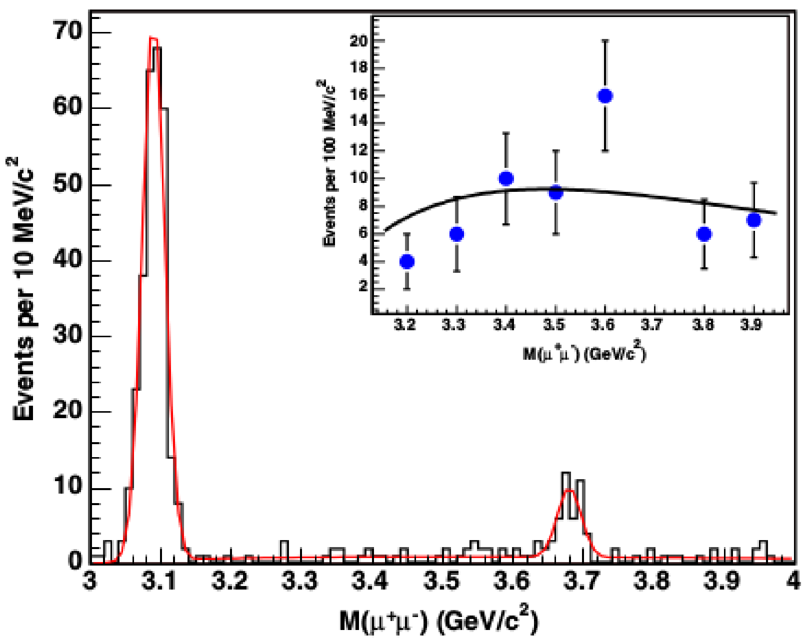

Figure 4.5: Mass $M_{\mu^+\mu^-}$ distribution of 402 exclusive events fitted by two Gaussian functions for J/ψ and $\psi(2S)$ and the QED continuum. In the inset are data excluding the J/ψ and $\psi(2S)$ with the fit to QED spectrum times acceptance.

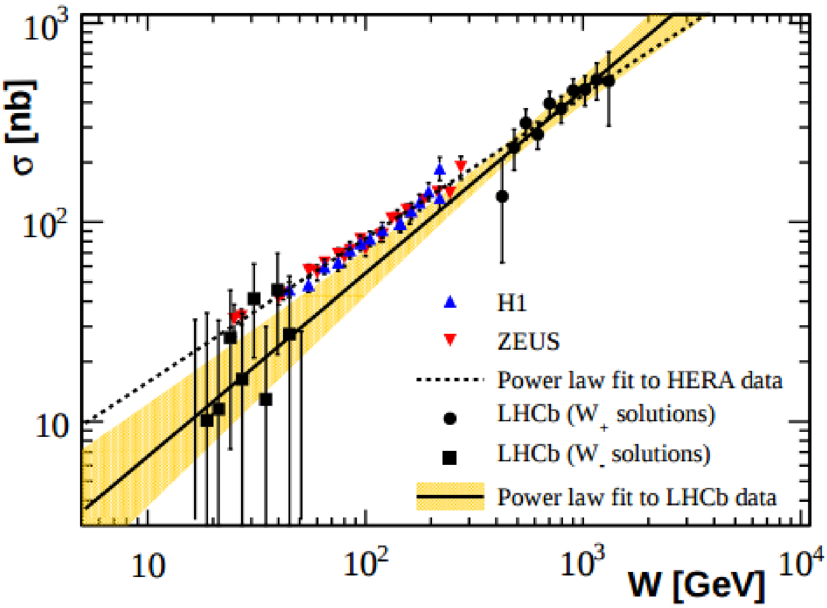

Figure 4.6: The total cross section of J/ψ photoproduction depending on $W_{\gamma p}$; centre of mass energy. The blue and red triangles represents the data from H1 and ZUES. The black squares and dots are data from LHCb. The dashed and full lines are the power law dependence determined from HERA and LHCb. The shaded band shows the uncertainty on the LHCb power law determination.

Chapter 5

Detector description

5.1 General description of ALICE detector

The detector used for this analysis is called A Large Ion Collider Experiment (ALICE) located at the Large Hadron Collider (LHC) in CERN. It is mainly focused on QCD, the sector of strong interaction in the Standard model. It is designed to study strongly interacting matter and quark-gluon plasma. Quark- gluon plasma, a state of matter when quarks and gluons are freed, at extreme values of energy density and temperature in nucleus-nucleus collisions. It allows a study of hadrons, electrons, muons and photons produced in collisions of heavy nuclei, up to the highest multiplicities anticipated at the LHC.The overall detectors dimensions are $16 \times 16 \times 26$ m^3 with a total weight of 10 000 tons. The detector consists of a central barrel part which covers polar angles from 45° to 135° and it is embedded in a large solenoid magnet of magnetic field $B = 0.5$ T, and a muon spectrometer covering the range of the pseudorapidity $-4 < \eta < -2.5$. The central barrel includes several central detectors which cover the pseudorapidity region $|\eta| < 0.9$. Those cylindrical detectors are used to track all the particles that fly out of the interaction. The Inner tracking system (ITS) is closest to the interaction point. It measures the location of the main collision and of the decay of particles which are short lived and decay quickly with a precision of a tenth of millimetre. The detector which surrounds ITS is called The time Projection Chamber (TPC). It is the main tracking device of charged particles and particle identification. Beyond the TPC is the Time Of Flight (TOF) detector. It is a large cylindrical barrel which gives very high precision timing for tracks traversing it. A full description of the detector and its performance can be found in [14, 15], here only the sub-detectors used for the analysis below will be briefly described.

5.2 Sub - detectors

5.2.1 Inner Tracking System

The Inner Tracking System (ITS) surrounds the beam pipe. It is the main contributor for measuring the primary vertex of the collision. The ITS consists of six layers of position sensitive semiconductor detectors. The innermost layers are Silicon Pixel Detectors (SPD). Beyond the SPD are two layers of Silicon Drift Detectors. The last two layers are Silicon Strip Detectors. These six cylindrical layers are shown in Figure 5.2.

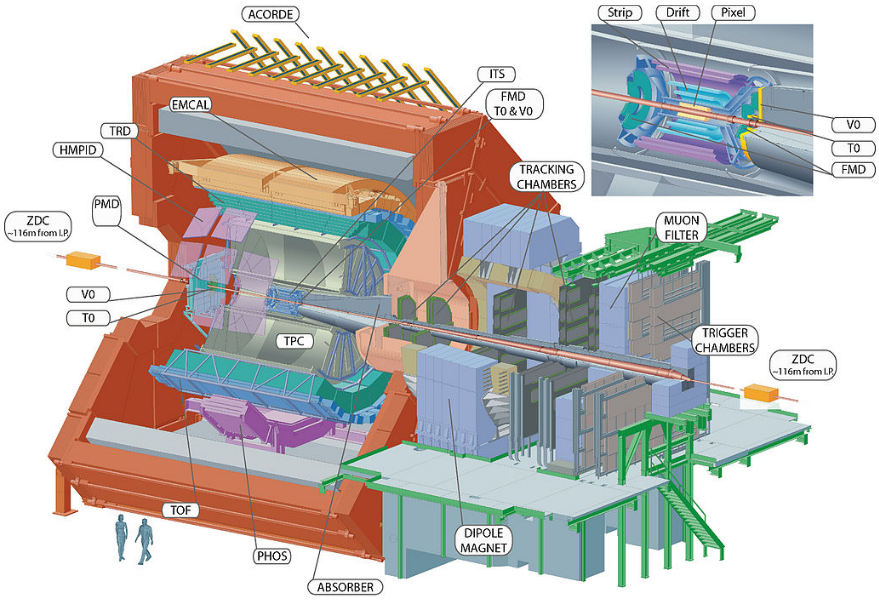

Figure 5.1: ALICE detector

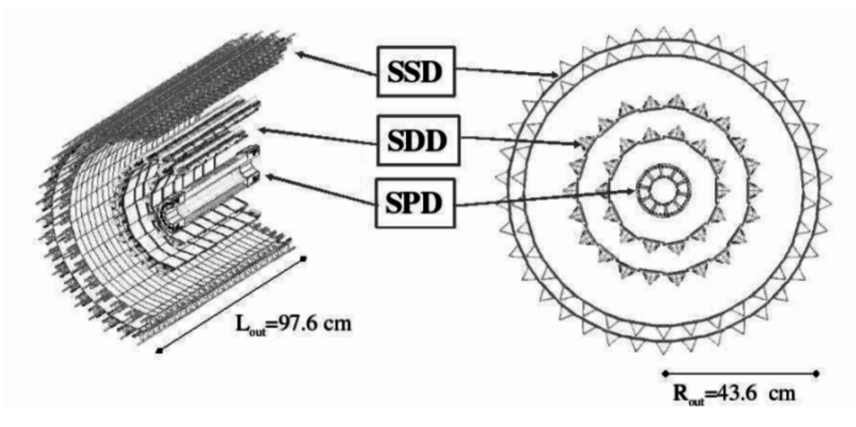

Figure 5.2: Layout of the Inner Tracking System.

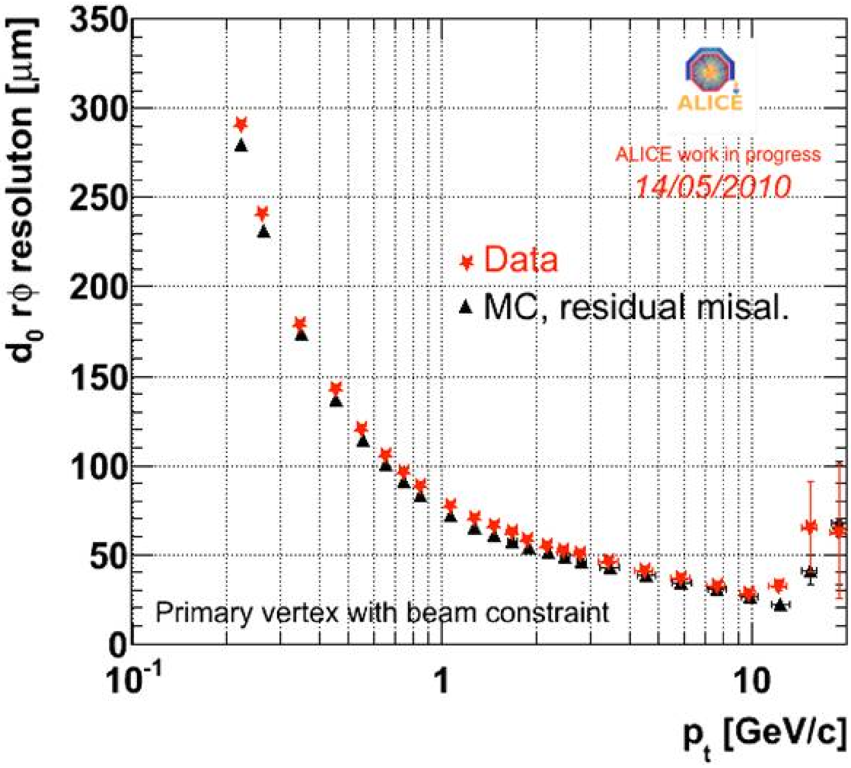

Figure 5.3: Transverse impact parameter resolution as a function of the particle transverse momentum, obtained for well reconstructed tracks having two measured point in the SPD. The resulting impact parameter resolution is the convolution of the track position and the primary vertex resolution. Data (Red stars) come from 2010 $Pb-Pb$ dataset. It is shown with comparison of Monte Carlo simulation (Black triangles).

The ITS is located at radius between 4 and 43 cm around the beam pipe. The detector layout has been designed taking into account the high multiplicity environment foreseen for central $Pb-Pb$ collisions, so that the occupancy is kept on the order of few percent.

The SPD, the two innermost layers of the ITS, is aimed to determine the position of the primary collision vertex with a resolution better than $100\mu m$. It has $9.8 \cdot 10^6$ readout channels receive signals from the 20 half-staves of SPD. Each of them consists of 240 modules with 1200 readout chips. The SPD is very highly segmented so it has also been used for the trigger system, especially for the minimum bias event selection. It is also used for the triggering of UPC processes at mid rapidity.

The Silicon Drift Detector (SDD) is based on modules with a sensitive area of $70.17(r\phi) \cdot 75.26(z)$ mm^2, divided into two drift regions where electron move in opposite directions under a drift field of approximately 500 V/cm. The modules are mounted into ladders, the inner layer is structured of 14 ladders with 6 modules each and the outer layer of SDD composes 22 ladders with 8 modules each of them. The position of the particles along the z axis is reconstructed from the centroid of the collected charge along the anodes and the position along the drift r coordinate is determined from the measured drift time with respect to the trigger time. A precise knowledge of the drift speed is needed for this reconstruction. The drift speed is measured during calibration runs.

The two outermost ITS layers form the Silicon Strip Detector (SSD) which is a module consisting of one double-sided strip detector connected to two hybrids hosting the front-end electronics. The sensors have an active area of $73(r) \cdot 40(z)$ mm^2 and they are 300μm thick. Each sensor has 768 strips on each side which are almost parallel to the z axis direction. The innermost layer of the SSD is composed of 34 ladders with 22 modules each. The outer layer is made of 38 ladders, each of them is composed of 25 modules.

A high resolution on the impact parameter is important to reconstruct secondary vertices from hyperons and heavy flavour hadrons decay. In Figure 5.3, the transverse impact parameter resolution is shown as a function of p_T, measured in 2010 Pb-Pb collisions. The resolution is obtained for tracks with two signals in the SPD. The resolution in the $r\phi$ plane is nearly $50\mu m$ for particles with momentum $1GeV/c$. With higher momentum the resolution decreases.

Four outer layers have analogue readout, therefore they can be used as a particle identification via dE/dx measuring in non-relativistic region for low momentum particles ($p_T > 100$ MeV). Electron can be identified from 80 MeV/c up to 160 MeV/c with 2 *sigma* separation from π. Pions are separated from kaons up to 0.6 GeV/c and kaons from protons up to 0.8 GeV/c.

The ITS reconstruct tracks which transverse the dead TPC regions or very low momentum and short tile living particles which do not reach the TPC. Also it improves the momentum and angular resolution for tracks reconstructed by the TPC.

5.2.2 Time Projection Chamber

The Time Projection Chamber (TPC) is a 88 m^3 cylindrical detector filled with gas, shown in Figure 5.4 It serves for tracking and for particle identification by specific energy loss measurements. The pseudorapidity range is $|\eta| < 0.9$ and it covers full azimuthal angle. The overall length along the beam direction is 510 cm, the inner radius is 80 cm and the outer radius is 250 cm. A central electrode separates the two drift regions, providing an electric field. Charged particles traversing the detector ionise

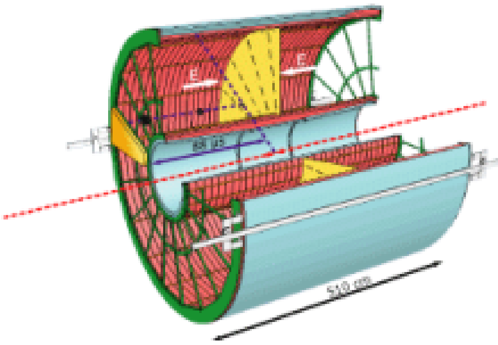

Figure 5.4: Time Projection Chamber

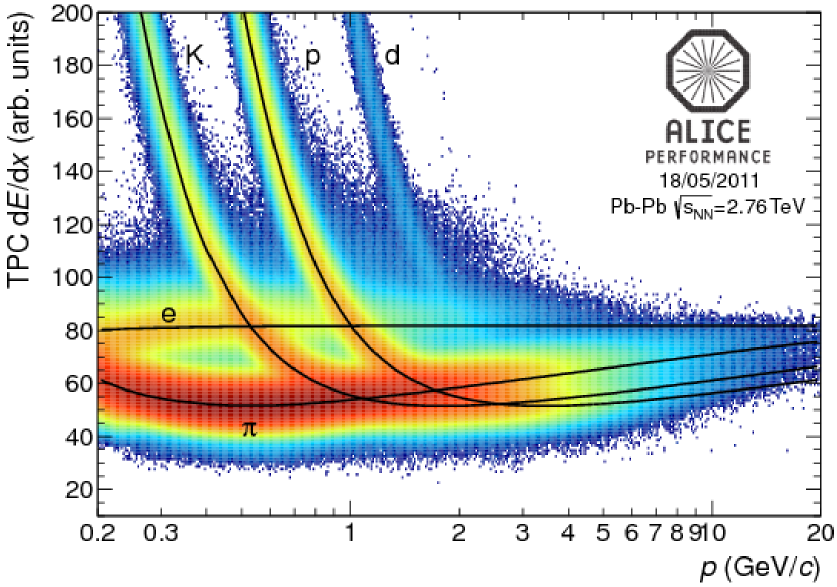

Figure 5.5: Energy loss distribution dE/dx of charged particles as a function of their momentum, measured by the TPC alone in $Pb-Pb$ collisions. The lines are a parameterization of the detector response based on Bethe-Bloch formula.

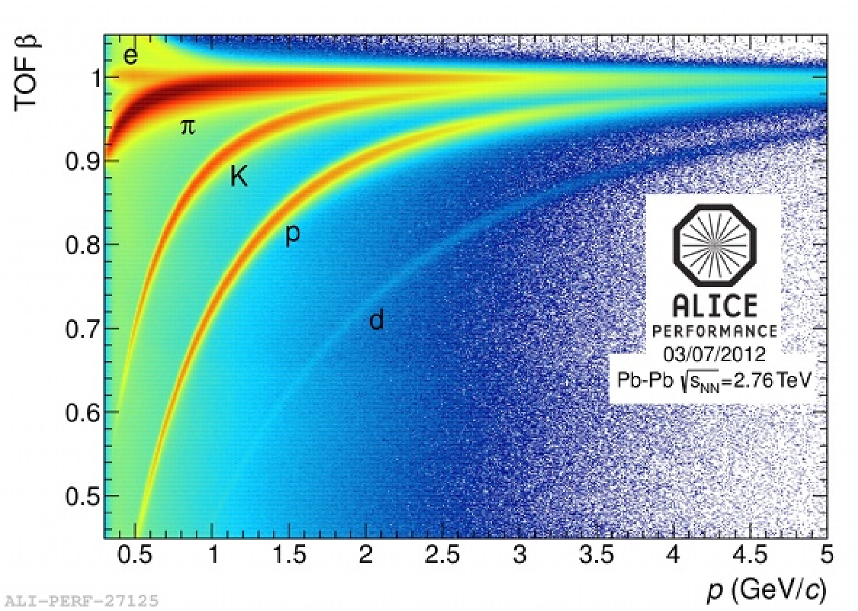

Figure 5.6: Correlation $\beta = v/c$ versus moomentum p as observed by TOF in $Pb - Pb$ collisions.

the gas and the liberated electrons drift towards the end plates of the cylinder. The end plates are divided in 18 sectors along the azimuthal angle they are made out of Multi-Wire-Proportional-Chambres (MWPCs) with 560 000 readout pads. It allows high precision track measurements. Although tracks from pile-up events can be rejected using cuts on the primary vertex position and arrival time, this one of the main factors that also forces ALICE to run at lower instantaneous luminosity with respect to the other LHC experiments. Another limiting factor is the long TPC dead time, that slows down the readout frequency despite the fact that the slowest detector is the SDD.

The TPC can track particles in a wide momentum range, (0.1GeV/c$< p_T < 100$ GeV/c), with a good momentum resolution and efficiency $> 90\%$ for $p_T > 100MeV$. The ITS and TPC are able to determine the momentum of the charged particles with a resolution better than 1% at low p_T and better than 20% for transverse momentum $p_T \sim 100GeV/c$. The charge collected in the TPC readout pads is used to measure particle energy loss dE/dx. Measured momentum and energy loss is used to identify various particle species in the low momentum region ($p_T < 1GeV/c$). In Figure 5.5 is shown the particle identification where the energy loss distribution for different charged particles is fitted by a Bethe-Bloch function.

5.2.3 Time Of Flight Detector

The Time Of Flight Detector (TOF) is a detector placed beyond the TPC. The TOF identifies charged particles in the intermediate momentum range. It is a large cylindrical barrel situated 3.7 m from the beam line. Its polar angle acceptance is 45°- 135°and it covers full azimuthal angle. The TOF detector is divided into 18 sectors in ϕ angle and into 5 segments in the direction of the beam axis. The external radius of the whole detector is 399 cm and the internal one is 370 cm. The pseudorapidity coverage is the same as for the TPC. The detector is instrumented with double-stack Multigap Resistive Plate Chambers (MRPCs) with more than 150 000 readout channels. It gives very precise timing for the tracks traversing it. The overall time of flight resolution of the TOF detector in Pb–Pb collisions reaches value of about $\sigma_{TOF} = 80$ ps. In conjunction with the momentum and track length measured by the ITS, the time measurements by the TOF are used to calculate the mass of the particle.

The TOF measures the β factor of a particle by the independent measurements of the time of flight t and the length L of its trajectory, from the vertex of the production to the sensitive element of the timing system. The momentum threshold for the detector is ~ 450 MeV/c for protons and antiprotons. With the momentum known it is possible to obtain an indirect measure of the mass of the particle. For a particle, which has the momentum p, the length of trajectory L and the time of flight t, the mass can be calculated by the formula (5.1).

$$m = \frac{p}{\beta\gamma_L} = p\sqrt{\frac{t^2}{L^2} - \frac{1}{c^2}} \tag{5.1}$$

As it is shown in Figure 5.6 the TOF separates pions from kaons at 3σ up to transverse momenta about 2.5 Ge/c and protons from kaons up to 4 GeV/c. To distinguish two particles with the same p and L, the the difference between the two times of flight has to necessarily be larger than the measure resolution. The capability to distinguish these two particles is called separation and it is expressed in terms of number of sigma.

As it was said the TOF exploits the MRPCs technology, capable of an intrinsic time resolution better than $\sigma_{MRPC} \sim 50$ ps with an efficiency close to 100%. The MRPC are ionisation chambers and each of them is formed by two parallel resistive plates (the anode and the cathode). The TOF double-stack MRPC consists of 10-gaps double-stack MRPC strip 122 cm long and 13 cm wide. The active area of $7.4 \cdot 120$ cm^2 is segmented in 96 readout pads, each of $3.5 \cdot 2.5$ cm^2.

5.2.4 V0 detector

The V0 is a detector consisting of two arrays of plastic scintillator counter installed on both sides of the interaction point. Those two counters are called V0A and V0C. It is a small-angle detector with the pseudorapidity coverage $2.8 > \eta > 5.1$ for V0A and $-3.7 < \eta < -1.7$ for V0C. The V0A array is installed on the positive z-direction about 340 cm from the interaction point. The detector is put inside a box of two equal halves which has 100 cm in diameter and 60 mm in thickness. The beam pipe goes trough the centre of the box. On the other side of the interaction point at distance of 900 mm stays the V0C detector. It is also closed in similar box unless this one is a little bit smaller (76 cm in diameter and 47 mm in thickness). Both arrays were constructed as large as possible, according to the other parts of the ALICE detector, to cover as large pseudorapidity range as possible. The V0 detector is divided into several counters as it is shown in Figure 5.7 . Each array consists of 32 counters distributed in 4 rings. Each ring is divided into 8 sectors in V0A and for V0C two outer rings are divided into 16 sectors. Each ring covers 0.5 - 0.6 units of pseudorapidity. When a particle hits the detector it produces a scintillation light which is converted by wavelength shifting fibres (WLS) and transported to photomultipliers.

This detector is used for its several functions. It provides minimum bias triggers for central barrel detectors in pp and Pb–Pb collisions together with SPD and the centrality triggers. These triggers are obtained from a large number of particles crossing the

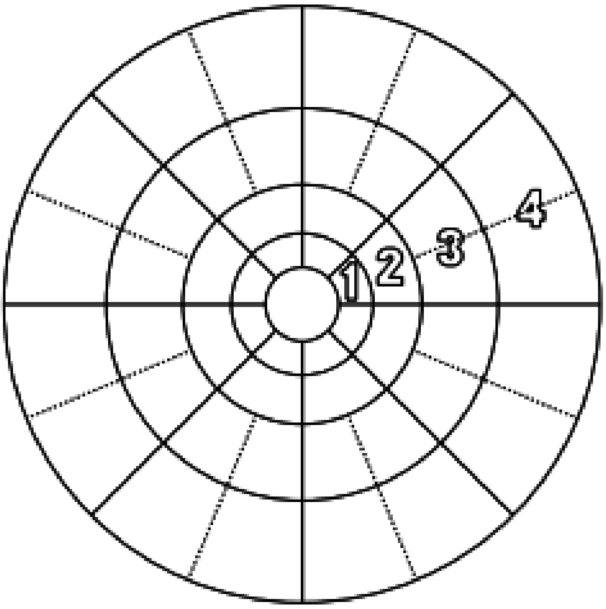

Figure 5.7: Segmentation of V0A(V0C) arrays. Additionally the V0C is segmented by the dashed line.

detector from initial collisions and also from the background of secondary interactions in the vacuum chamber elements. The V0 works as an indicator of the centrality of the collision through the multiplicity recorded in the event provided the dependence between the number of registered particles in the V0 arrays and the number of primary emitted particles remains monotone. Cut on the signal can be applied to achieve rough centrality triggers such as the multiplicity, semi-central and central triggers.

5.2.5 ZDC

In Zero degree calorimeter non-interacting (spectators) nucleons are detected. By measuring the energy of spectators, we can determine the centrality of the collision. Two

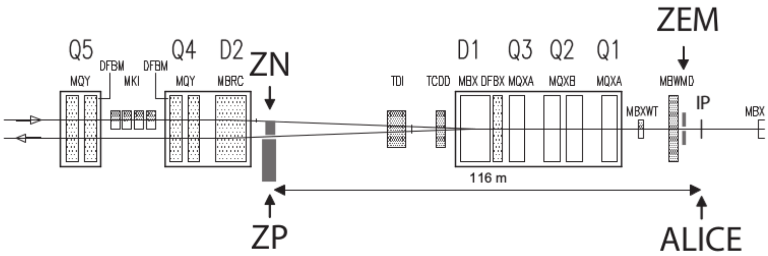

Figure 5.8: Schematic top view of beam line of ALICE. Location of proton (ZP), neutron (ZN) detectors and forward electromagnetic calorimeter (ZEM) are shown.

sets of ZDCs are installed at 116 m from both sides of the beam interaction point. We can measure non-interacting protons or neutrons. Protons and neutrons are separated by the magnetic field of the beam line. The ZDC is made out of two different detectors. The spectator neutrons are measured by the ZDC detector placed between the beam pipe at 0° with respect to the beam direction. The detector for the spectator protons is installed externally to the outgoing beam pipe, see the Figure 5.8.

The energy resolution of the ZDC detectors must be comparable with the spectator energy fluctuations for a given impact parameter. ZDCs are placed very close to the beam so the transverse size of the detectors is constrained. Therefore the hadronic ZDC are made of quartz fibres as active material. The charged particles from the shower generated in the absorber produce Čerenkov radiation in quartz fibres and it is sent to the photodetectors. Čerenkov calorimeters provide a very fast signal, due to the intrinsic speed of the Čerenkov emission process. The ZDC detector is used for triggering purposes, such as centrality trigger. Two small electromagnetic calorimeters (ZEM) are placed at about 7 meters from the interaction point on both sides. They are used in particular to distinguish central from peripheral and ultra-peripheral collisions. In central collision a small amount of energy is deposited in the ZDCs. But it could be also observed for UPCs, where spectator nucleons can bound into fragments which do not get out of the beam pipe and can not be detected from the hadronic calorimeters. The ZEM allows to distinguish between events with different centrality by measuring the energy of the particles emitted at forward rapidity that increases with the collision centrality.

Chapter 6

Analysis of J/ψ and the results

In this chapter the results of my work are presented. It is the first exploration of J/ψ decaying into $p\bar{p}$ in UPCs in ALICE. First part of the chapter is concentrated on used Monte Carlo dataset description and the triggers which were used for this analysis. Then the selection criteria are presented and efficiency and acceptance is estimated. The kinematic distributions of the J/ψ and the mass resolution for selected events are presented and compared to the previous ALICE results. Finally, number of candidates that can be measured during the Run 2 is calculated.

6.1 Event $J/\psi \rightarrow p\bar{p}$ display in the detector

An event with exclusively produced J/ψ is experimentally determined very clearly. Only two tracks are reconstructed in otherwise empty detector. The J/ψ products might be $\mu^+\mu^-$, e^+e^- or $p\bar{p}$ pair. This analysis focuses on the $p\bar{p}$ production. Figure 6.1 shows an event display for a J/ψ candidate produced in Pb–Pb UPCs at $\sqrt{s_{NN}} = 2.76$ TeV.

6.2 Coordinate system and kinematic variables

The coordinate system used in ALICE is as follows: the z-axis (longitudinal direction) is set up to be parallel to the beam direction and the x-y plane is transverse to the beam direction. The centre of coordinate system is in the interaction point (IP). The positive direction of the z-axis is defined so the right-handed coordinate system is created. The positive x-axis points from IP to the centre of the LHC ring and positive y-axis is defined as pointing upwards.

The angle measured around the beam axis is determined as azimuthal angle ϕ and polar angle θ is the angle between the beam axis and the measured point.

To measure kinematics of the particle following term are defined:

The rapidity y is defined as:

$$y = \frac{1}{2} ln \frac{E + p_z}{E - p_z} \tag{6.1}$$

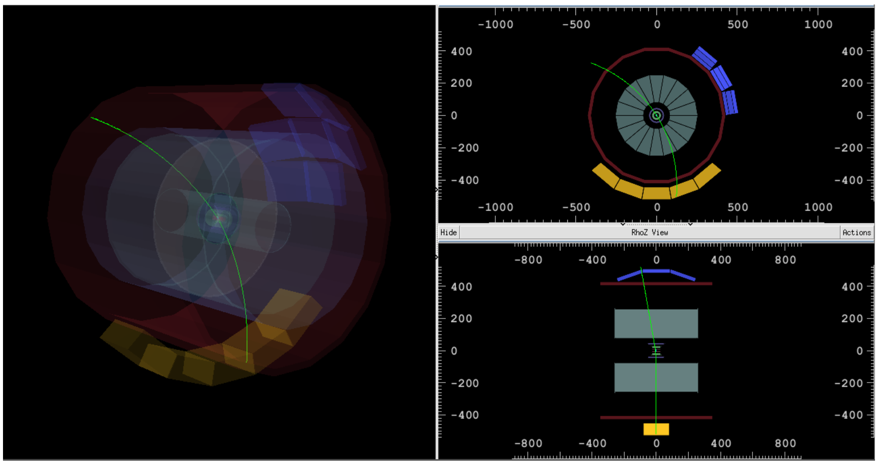

Figure 6.1: Event display of J/ψ decaying into $p\bar{p}$ generated in a Pb–Pb UPC with Starlight and passed through a full Geant simulation of the ALICE detector.

and pseudorapidity is given by the equation:

$$\eta = -ln \tan \frac{\theta}{2} \tag{6.2}$$

6.3 Used Monte Carlo data

In this analysis used data was simulated by the Monte Carlo (MC) program for RUN1 and they are used to calculate acceptance and the efficiency for triggering, track reconstruction, event selection and $p\bar{p}$ identification.

The J/ψ signal events are generated by the STARLIGHT which is based on the Vector Dominance Model. The STARLIGHT is an event generator for UPCs. The program produces a different vector meson for each relevant event and the particles which the particular vector meson decays into. For the ALICE detector response on those particles GEANT3 is used. The data was analysed using ROOT software. From this dataset a ROOT tree was produced just as done for real data.

6.3.1 STARLIGHT generator and selection

The total STARLIGHT cross section for J/ψ in Pb–Pb UPCs at centre-of-mass energy $\sqrt{s_{NN}} = 2.76$ TeV is 23.162 mb. The generated J/ψ have been filtered to rapidity $-1.0 < y < 1.0$. The decays of J/$\psi \rightarrow p\bar{p}$ have been generated assuming the transversal polarisation for the J/ψ and events with tracks pseudorapidity in range $-1.2 < \eta < 1.2$ were selected.

This analysis uses simulated data to runs: 168065, 168076, 168511.

The number of generated events was 9000 for each run.

In the analysis over the ESDs, the tracks were selected to have:

- At least one point in SPD.
- At least one TPC cluster.
- ITS refit.
- TPC refit.
- Two tracks only with unlike-sign.

In total 5742 events were selected and written to the ROOT tree out of 27000 simulated events.

6.4 Selection criteria of events

It was shown, in Chapter 3, how ultra-peripheral events are characterised by an event topology. Coherently produced J/ψ are characterised by very low transverse momentum and their decay implies a back-to-back track configuration, with no other tracks due to the absence of hadronic interactions. These events can be detected requiring only two well-reconstructed tracks in an otherwise empty detector.

6.4.1 Track selection

It is required to have two reconstructed tracks with following selection criteria:

- Each track has at least 70 TPC clusters.
- χ^2 is less than 4 in TPC.
- Each track has $|\eta| < 0.9$.

From 27 000 generated events it was selected 4806 reconstructed events.

6.4.2 Trigger selection

We want to explore the efficiency of using the CCUP4 trigger, built with information from SPD, VZERO and TOF. The reconstructed events have to satisfy following conditions:

- 0SM2 from SPD: At least two fired chips on SPD outer layer.
- 0OMU from TOF: Between 2 and 6 fired sectors at TOF and at least two of them back-to-back, it is a condition of the azimuthal difference $150^\circ < \Delta\phi < 180^\circ$
- Veto from V0A and V0C: no hits in the V0 detectors both from A side and C side.

A total number of events that have satisfied all of these requirements is 1339.

Because it was selected very few of events I used also a sample of events that have satisfied the 0SM2 trigger only. By this selection I got 3616 event. The efficiency of the TOF detector will be calculated in following parts.

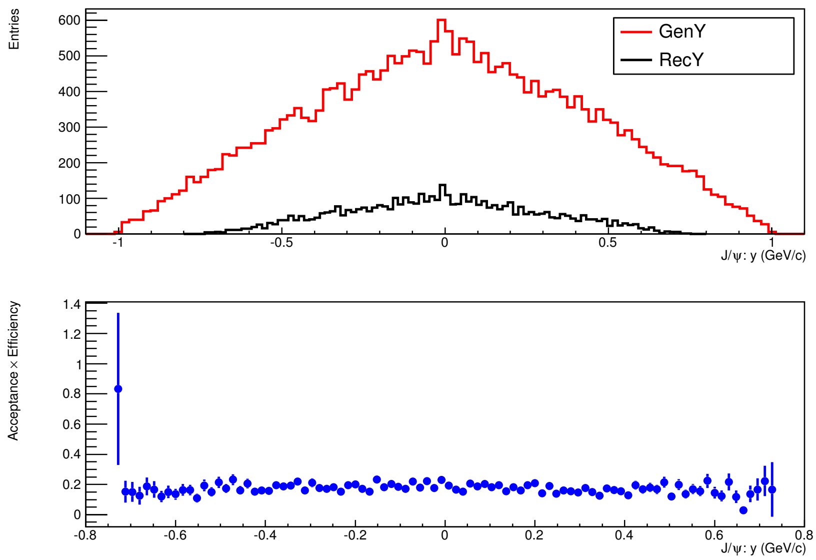

Figure 6.2: Acceptance $\times$ efficiency for the rapidity distribution. The upper histogram shows the rapidity distribution of events that satisfy all the selection criteria (black line) and the Monte Carlo generated (red line) events. The histogram bellow visualises the acceptance and efficiency.

6.5 Acceptance and efficiency

In this part I calculate the acceptance and efficiency of the detector and SPD and TOF detector separately. I include the histograms of distributions for y, p_T and ϕ dependence and and its ratios. The possible reasons of acceptance and efficiency loss are discussed.

6.5.1 Acceptance and efficiency of the detector

The Monte Carlo simulated data are used to calculate the acceptance and efficiency of $J/\psi \rightarrow p\bar{p}$ decay. Since in the detector are some blind spots and the detector does not cover 100%, some of the events are not recorded. The number of recorded events by the detector is reduced by the acceptance and efficiency of the detector. The actual number of events that hit the detector and hence are recorded is the efficiency. The loss of events that slip through the blind spot is due to the acceptance of the detector.

The efficiency and acceptance ($A \times \varepsilon$) of the detector is computed as the ratio of the events which passes through the selection criteria, and the events which were generated by the STARLIGHT generator:

$$A \times \varepsilon = \frac{N_{reconstructed}}{N_{generated}}$$

The acceptance $\times$ efficiency of the detector was computed as:

$$A \times \varepsilon = \frac{N_{reconstructed}}{N_{generated}} = \frac{4806}{27000} = 0.178$$

for the rapidity and the p_T distribution. The acceptance and efficiency of the detector is 17.8%. The rapidity and p_T distributions and ratios are shown in Figures 6.2 and 6.3.

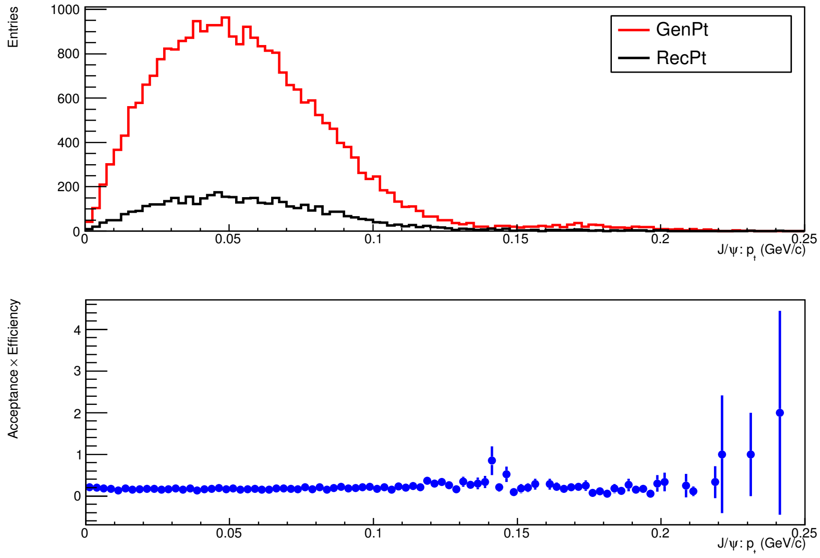

Figure 6.3: Acceptance $\times$ efficiency for the transverse momentum distribution. The upper histogram shows rapidity distribution of events that satisfy all the selection criteria (black line) and the Monte Carlo generated (red line) events. The histogram bellow visualises the acceptance and efficiency.

6.5.2 Efficiency and acceptance of the used triggers

The acceptance and efficiency of the trigger is computed as the ratio of the events which satisfy the conditions of the trigger, and the events reconstructed by the selection criteria. First the acceptance and efficiency of the 0SM2 trigger was computed as $75,2\%$. $A \times \varepsilon_{SPD} = \frac{N_{0SM2}}{N_{reconstructed}} = \frac{3616}{4806} = 0.752$
In Figures 6.4, 6.5 and 6.6 the y, p_T and ϕ distributions for selected trigger and their ratios are shown. The loss of events is due to geometrical properties of the SPD detector. From the histograms it is visible that there is no dependence of the acceptance and efficiency on the kinematics of the J/ψ.

Next we calculate the ratio: $A \times \varepsilon_{TOF} = \frac{N_{0SM2+0OMU}}{N_{reconstructed}} = \frac{1339}{4806} = 0.279$ shows that it does not happen. Almost 2/3 of events get lost. In Figures 6.7, 6.8 and 6.9 the ratios of events that were reconstructed with SPD and TOF detector and all reconstructed events are shown in dependence on P_T, y and ϕ. The acceptance and efficiency of the TOF detector $A \times \varepsilon_{TOF} = 27.9\%$ is very low. Possible reason of this considerable loss of events is that the tracks were not back-to-back as required by the CCUP4 trigger. I created a histogram (Figure 6.10) where I did a difference of angular distribution ϕ_1 of one track and the ϕ_2 of the second track. From the spectra it is clearly visible that produced $p\bar{p}$ pairs are back-to-back.

The TOF detector has a large coverage for tracks with $|\eta| < 0.9$, so we had no explanation for this low efficiency during the RUN1. Unfortunately there was no information in the tree that allowed us to study this further. A more in depth study would require more time and it is thus outside the scope of this work.

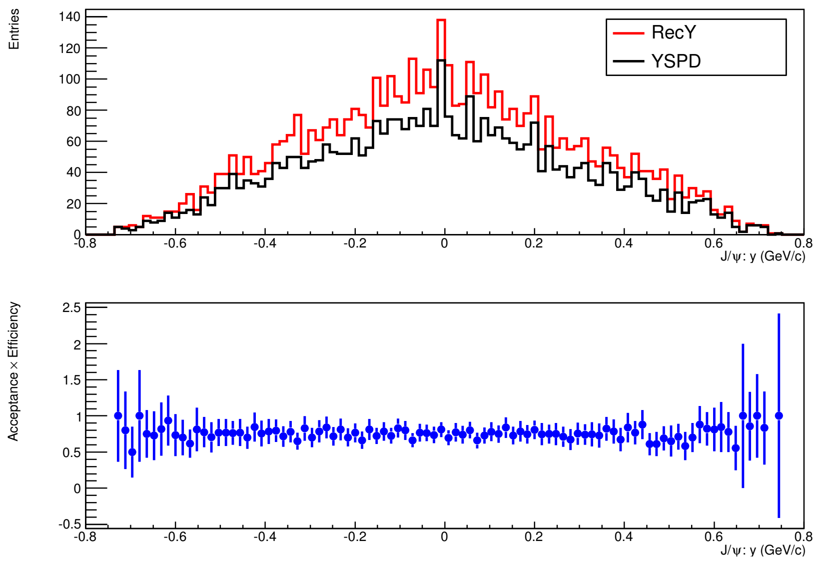

Figure 6.4: y distribution of reconstructed events (red) and events recorded by the SPD detector (black). The lower histogram shows acceptance $\times$ efficiency of SPD detector in dependence on rapidity y.

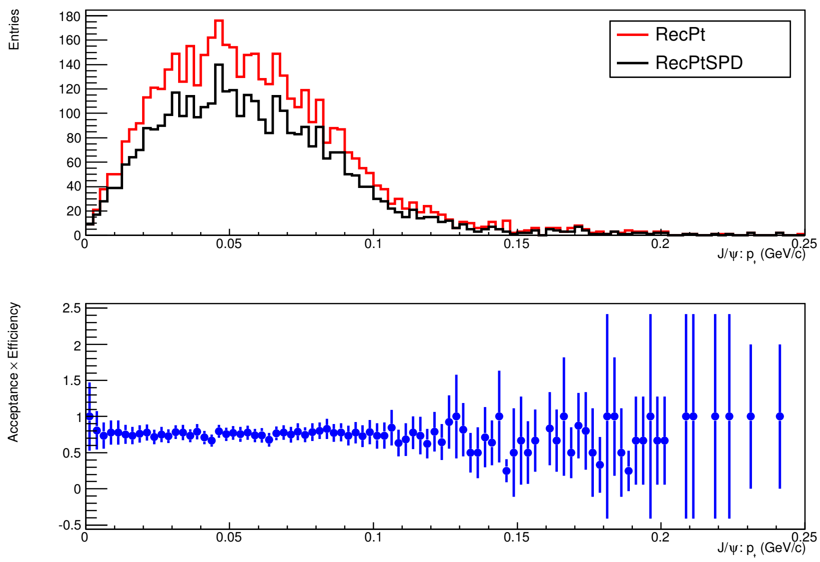

Figure 6.5: p_T distribution of reconstructed events (red) and events recorded by the SPD detector (black). The lower histogram shows acceptance $\times$ efficiency of SPD detector in dependence on transverse momentum p_T.

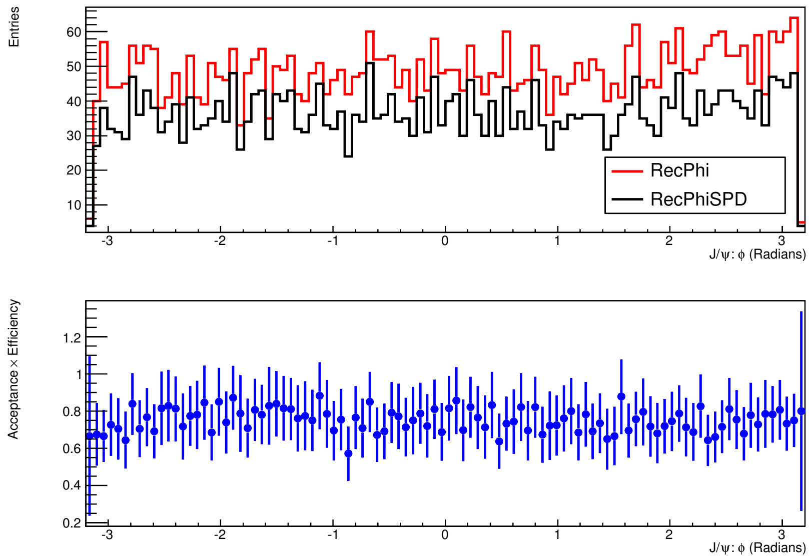

Figure 6.6: ϕ distribution of reconstructed events (red) and events recorded by the SPD detector (black). The lower histogram shows acceptance $\times$ efficiency of SPD detector in dependence on ϕ.

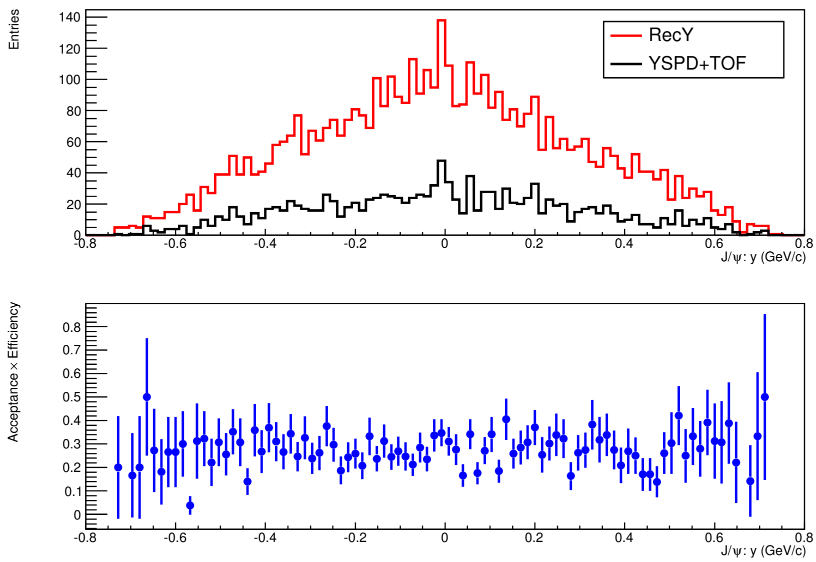

Figure 6.7: Acceptance $\times$ efficiency for the rapidity distribution. The upper histogram shows the rapidity distribution reconstructed (red) events and events that where recorded by the SPD and also the TOF detector (black). The histogram bellow shows the ratio of these two distributions.

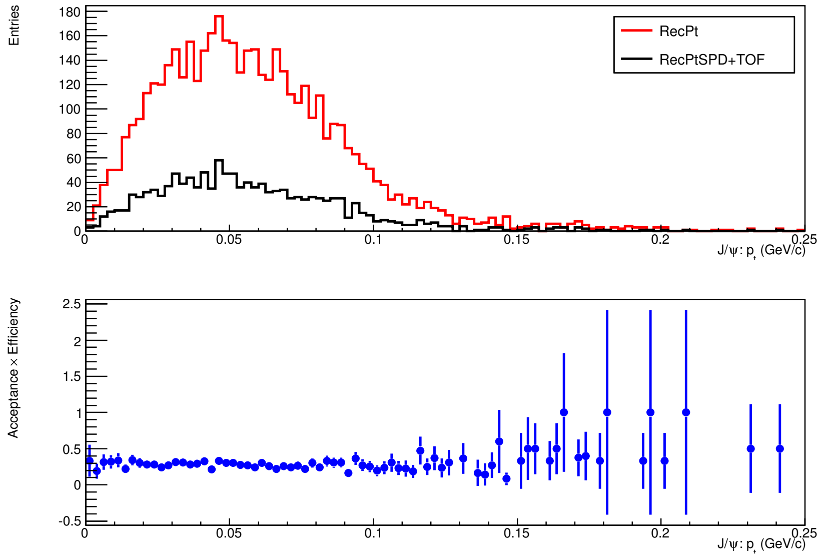

Figure 6.8: Acceptance $\times$ efficiency for the p_T distribution. The upper histogram shows the rapidity distribution reconstructed (red) events and events that where recorded by the SPD and also the TOF detector (black). The histogram bellow shows the ratio of these two distributions.

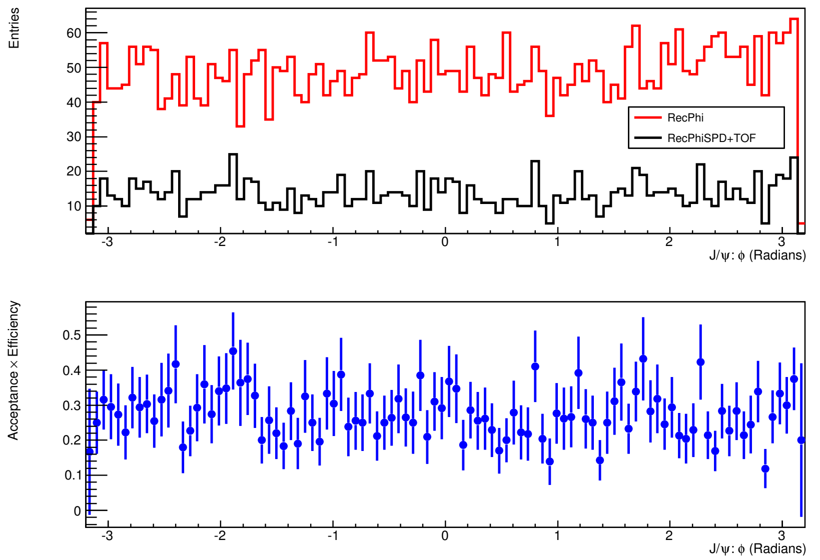

Figure 6.9: Acceptance $\times$ efficiency for the ϕ distribution. The upper histogram shows the rapidity distribution reconstructed (red) events and events that where recorded by the SPD and also the TOF detector (black). The histogram bellow shows the ratio of these two distributions.

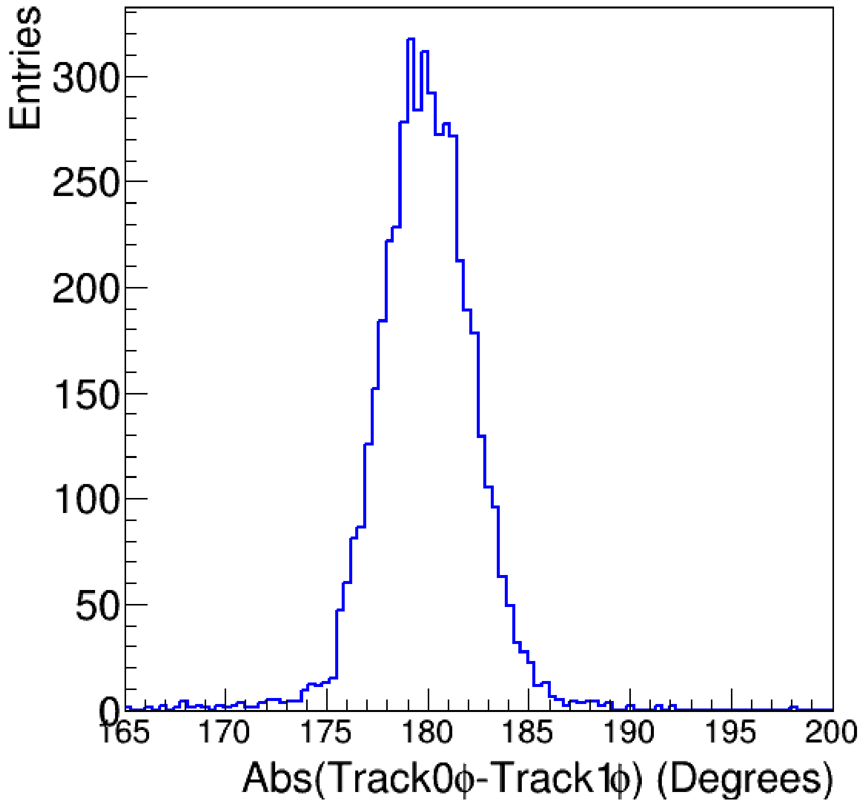

Figure 6.10: Δ_ϕ difference in degrees for produced $p\bar{p}$ pair in the event. On the x-axes are degrees in range $165^\circ < \Delta_\phi < 200^\circ$, the y-axis shows number of entries.

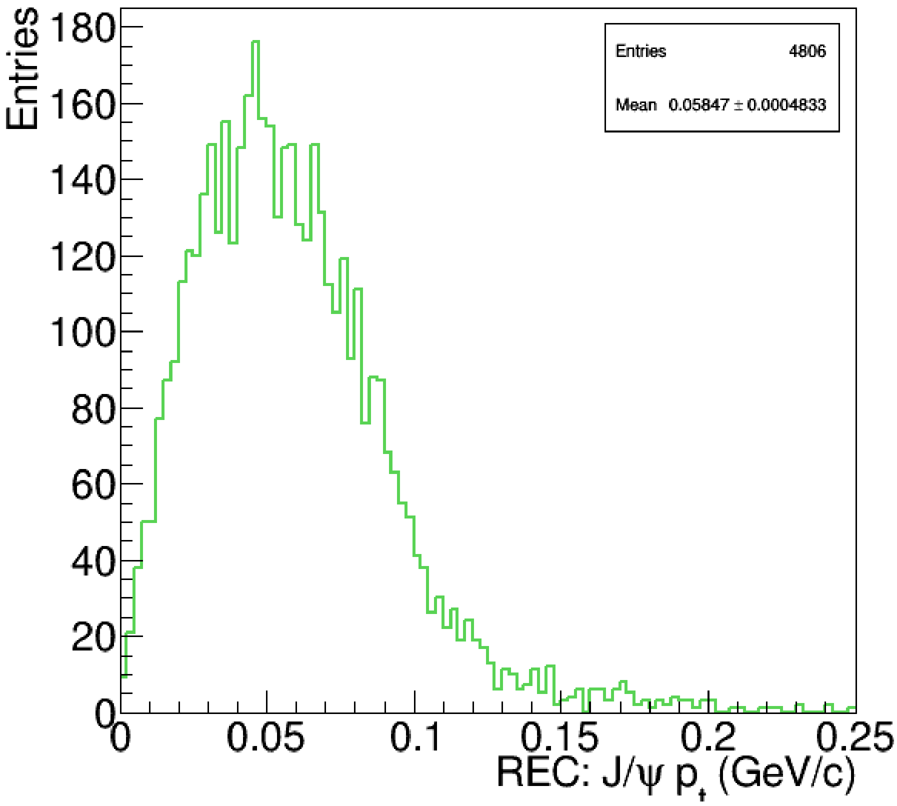

Figure 6.11: The transverse momentum distribution of the reconstructed coherently produced $J/\psi \rightarrow p\bar{p}$ in range $0 < p_T < 0.25$ GeV/c.

6.6 Kinematic distributions of J/ψ

The kinematic distributions of J/ψ are presented and described in this section.

For coherently produced J/ψ it is characteristic to have low transverse momentum, around $p_T = 60$ MeV. Studying the Figure 6.11 the peak in about $p_T = 50$ MeV is clearly visible. Because of the narrow peak and absence of J/ψ produced in higher p_T we can talk about coherently produced J/ψ.

In Figure 6.12 the rapidity distribution for $J/\psi \rightarrow p\bar{p}$ is shown. For the rapidity cut $-0.8 < y < 0.8$ was used. The J/ψ are produce in central rapidity.

The ϕ distribution is figured in 6.13. We can confirm that in average the same number of J/ψ is produced in each angle.

6.7 Kinematics of the p and $\bar{p}$ tracks

In Figure 6.14 the spectra of decay pair $p\bar{p}$ in dependence on the p_T, ϕ and η are shown. Both positive and negative particles follow the same shape of the kinematic

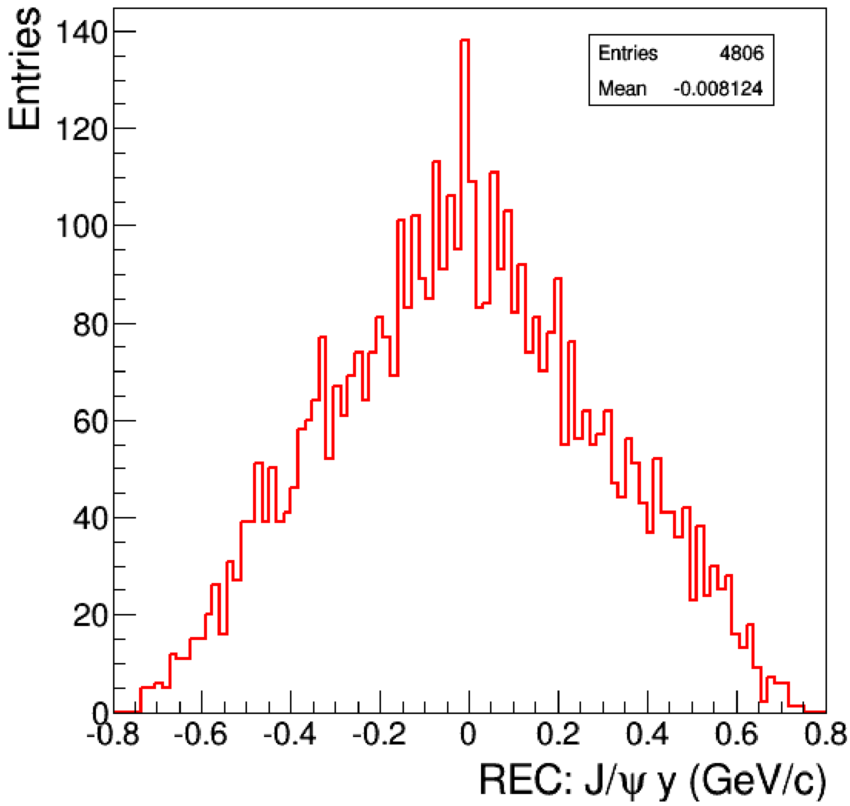

Figure 6.12: The rapidity distribution of the reconstructed J/ψ in range $-0.8 < y < 0.8$.

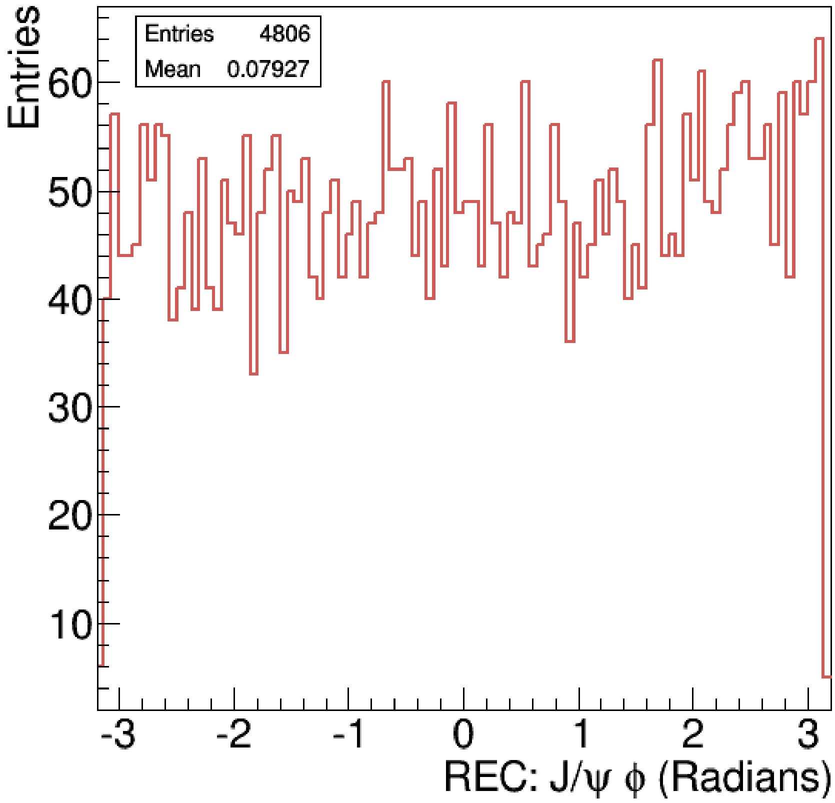

Figure 6.13: ϕ distribution of the reconstructed $\mathrm{J}/\psi \to p\bar{p}$.

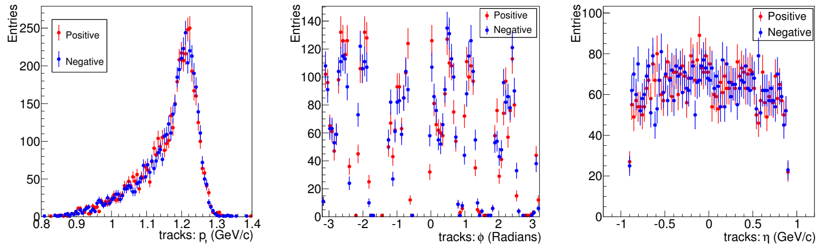

Figure 6.14: Distributions for tracks: left: the transverse momentum, middle: the azimuthal angle and right: pseudorapidity.

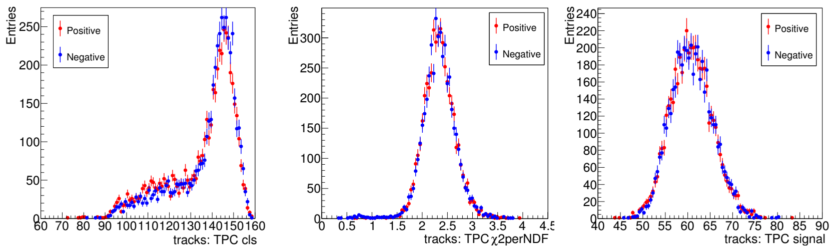

Figure 6.15: Distributions for TPC information of tracks: left: number of clusters, middle: χ^2 and on the right: TPC dE/dx.

distributions. It is what was expected because p and $\bar{p}$ have the same properties and they behave the same going through the detector.

In the track selection was used a cut that the number of TPC clusters must be more than 70 and the $\chi^2 < 4$. In Figure 6.15 is shown that almost all of the event fulfil the selection. In the figure the spectrum of the TPC signal for $p\bar{p}$ tracks is visualised. These spectra include all reconstructed events.

For the events that satisfied all the trigger selection criteria mentioned above, the properties of tracks might slightly differ. Studying Figure6.16 there is a noticeable deviation in spectrum of number of TPC clusters for p and $\bar{p}$ particles. Also for the TPC signal proton (red points) seems to be a bit shifted to the right from antiprotons (blue points).

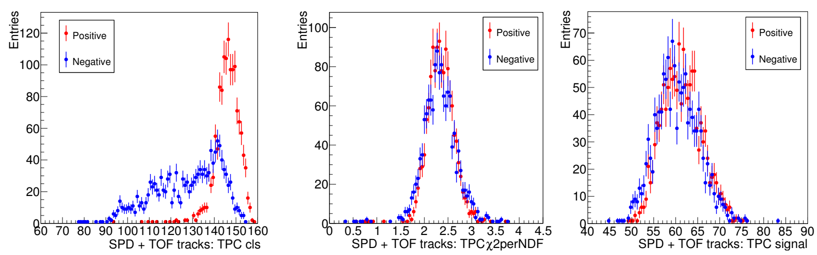

Figure 6.16: Distributions for TPC information of tracks that have SPD and TOF trigger information: left: number of clusters, middle: χ^2 and right: TPC dE/dx.

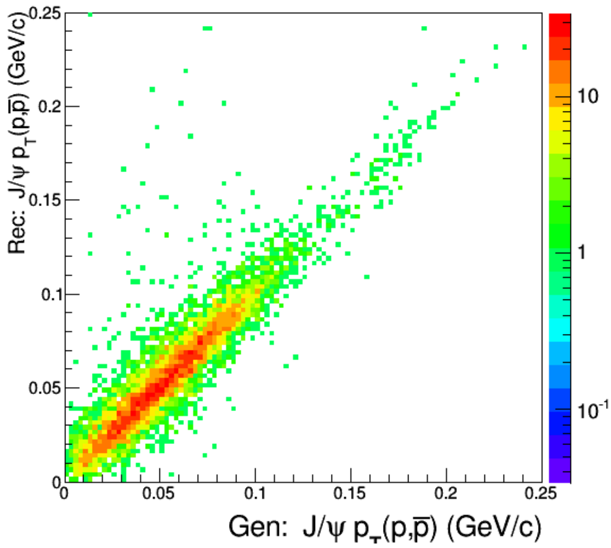

Figure 6.17: Two dimensional histogram of p_t distribution for reconstructed and generated events.

The two-dimensional histograms of J/ψ that were selected in dependence on J/ψ generated for p_T, y and ϕ variables can be seen in figures 6.17,6.18 and 6.19. It is apparent from the histograms that most of generated events with specific value of p_T, y or ϕ were also reconstructed with the same value. In the Figure 6.20 the projection for p_T distribution at $p_T = 0.025$ GeV and $p_T = 0.05$ GeV is shown. It was extracted from the Figure 6.17. The distribution is fitted by the Gaussian function. For the comparison I used histogram (Figure 6.21) created in the same way for the J/ψ decaying into $\mu^+\mu^-$ pair. It is clearly visible that both histograms are very similar, although in $p\bar{p}$ decay channel the σ is 15% better. Comparing these p_T projection to results from ALICE measurements, mentioned in chapter 4, Figure 4.1; [9], it is evident that the peak of the p_T projection is narrower than the peak of coherently produced J/ψ in ALICE measurements.

6.8 Mass resolution

The goal of this work was to assess if the mass resolution of the J/ψ decaying into $p\bar{p}$ pair is more precise than $M_{\mathrm{J}/\psi}$ measured in previous experiments, see chapter 4. Also part of our interests was if the mass peak of η_C meson would be possible to be seen.

η_C is a meson with a mass very close to the mass of J/ψ meson, $M_{\eta_C} = 2981.0 \pm 1.1$ MeV, and it is produced in a lesser extant than the J/ψ. Measuring the $\mathrm{J}/\psi \to l^+l^-$, where $l = \mu, e$ it is never possible to see the mass peak of η_C because of the long tail in the J/ψ mass distribution. This tail is due to ionisation of the lepton pair passing through the detector. However proton and antiproton are much heavier particles than leptons so they have larger speed and they do no ionise that much on their way through the detector. That is the reason why the narrow peak for the decay $\mathrm{J}/\psi \to p\bar{p}$

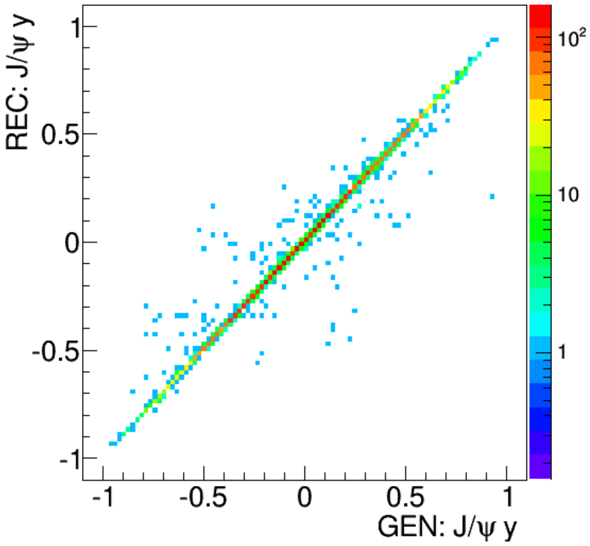

Figure 6.18: Two dimensional histogram of rapidity distribution for reconstructed and generated events.

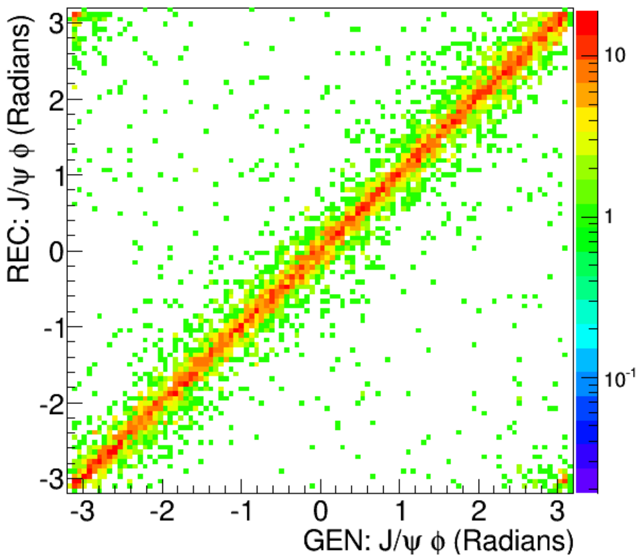

Figure 6.19: Two dimensional histogram of Φ distribution for reconstructed and generated events.

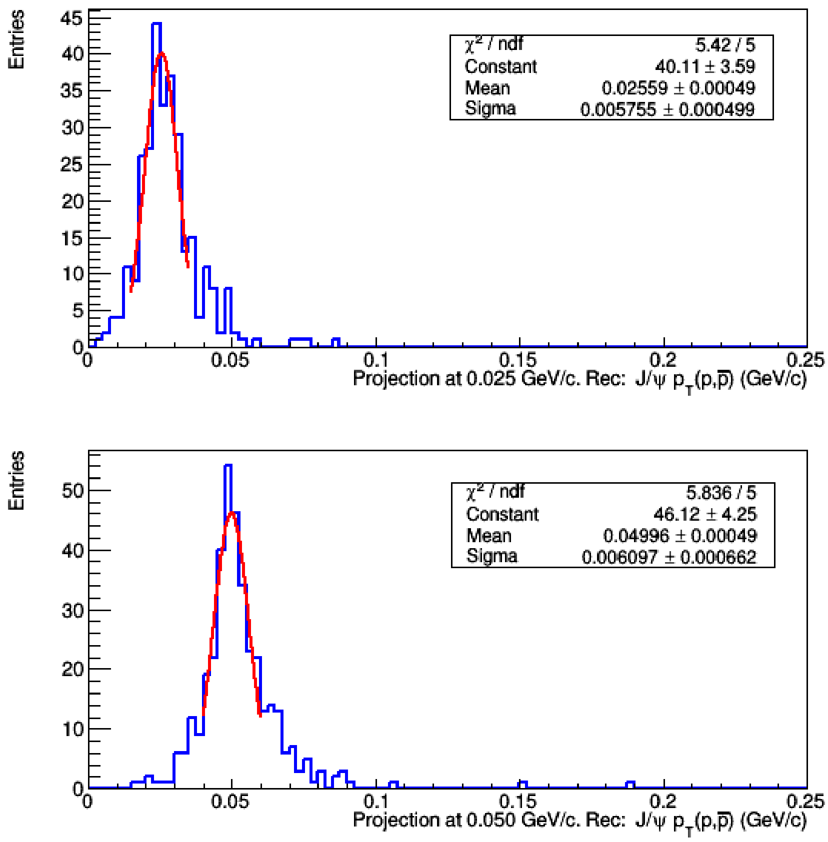

Figure 6.20: The projection for p_T distribution at $p_T = 0.025$ GeV and $p_T = 0.05$ GeV for $\mathrm{J}/\psi \to p\bar{p}$.

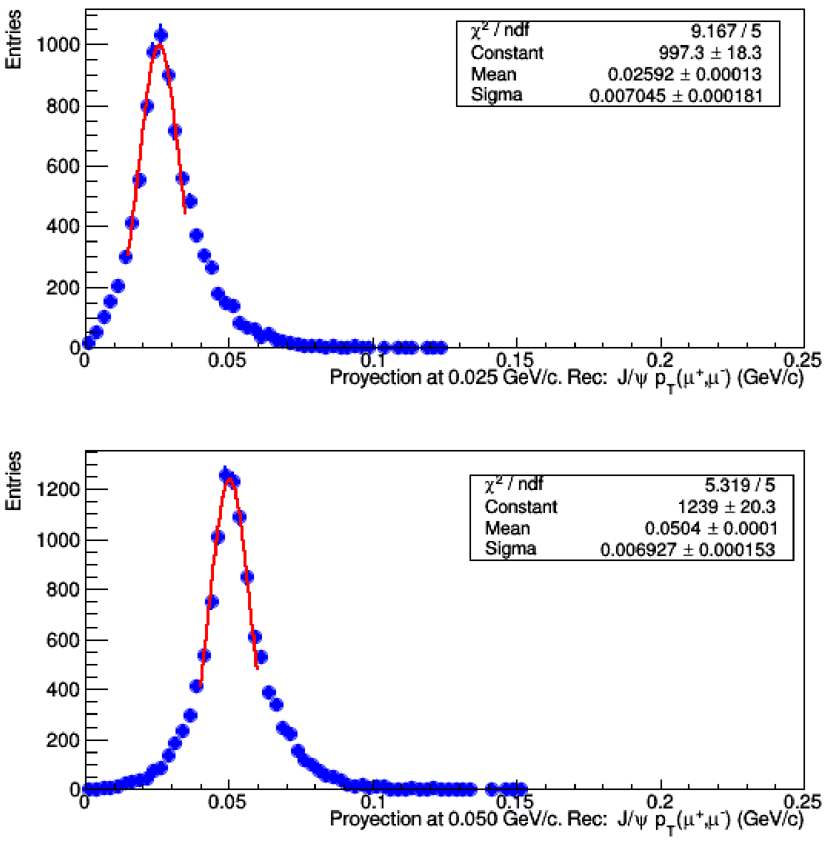

Figure 6.21: The projection for p_T distribution at $p_T = 0.025$ GeV and $p_T = 0.05$ GeV for $J\text{J}/\psi \rightarrow \mu_+\mu_-$.

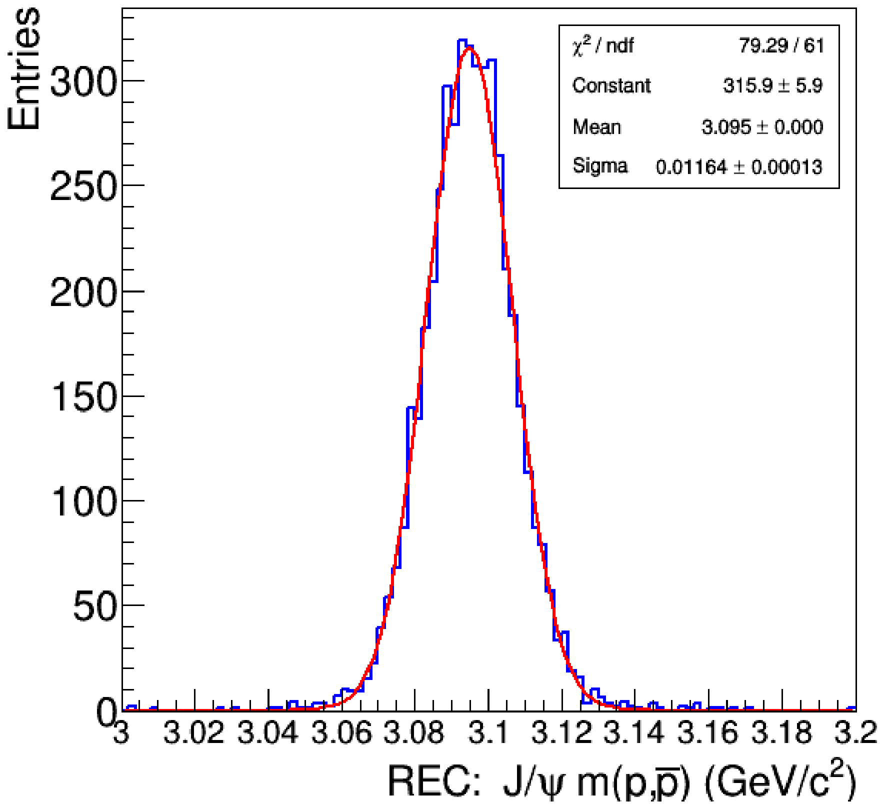

Figure 6.22: Mass of the reconstructed $\mathrm{J}/\psi_{p\bar{p}}$ in range $3.0 < M_{\mathrm{J}/\psi_{p\bar{p}}} < 3.2$ GeV/c^2, fitted by the Gaussian function.

is expected. The mass resolution of the measured $\mathrm{J}/\psi \to p\bar{p}$ is shown in Figure 6.22. The range of the mass is $3.0 < M_{\mathrm{J}/\psi_{p\bar{p}}} < 3.2$ GeV/c^2 and the distribution is fitted by the Gaussian function. The mass peak of η_C at $M_{\eta_C} = 2.98$ GeV would be clearly visible next to the mass peak of the J/ψ.

According to the article [9], Figure 4.2 one can see that the obtained precision is almost twice as better. The tail is missing because the $p\bar{p}$ pair do not interact with the detector as much as lepton pair. This has to be contrasted with the loss of statistics due to the different branching ratios.

6.9 Estimation of number of candidates

Table 6.1 summarises the effect of the different steps on the expected cross section.

During RUN1 the luminosity recorded with the CCUP4 trigger was 23 1/μb. According to STARLIGHT and the simulation we expect to find some 9 $\mathrm{J}/\psi \to p\bar{p}$ candidates in this sample. A preliminary analysis of these data was carried out in the UPC group of ALICE and without background subtraction 11 candidates were found in the mentioned channel and around 8 candidates in the $\mathrm{J}/\psi \to p\bar{p}\pi\pi$. The mass distribution

Table 6.1: Cross sections, according to STARLIGHT and the Geant simulation of ALICE, after the different steps of the selection procedure are applied.

Selection step	Cross section
Total cross section	23.16 mb
J/ψ: $\lvert y\rvert < 1$	8.3 mb
BR to $p\bar{p}$	17.9 μb
Generated $p/\bar{p}$: $\lvert\eta\rvert < 0.9$	7.8 μb
ESD preselection	1.7 μb
Selection	1.4 μb
VZERO veto	1.4 μb
0SM2	1.05 μb
00MU	0.4 μb

for these cases are shown in Figure 6.23. The prediction of STARLIGHT for coherent J/ψ production was smaller than what was measured by ALICE by a factor around 1.7. Given the small statistics all these values are consistent.

For RUN2 there is already some 135 1/μb of luminosity recorded during 2015 with a CCUP4 like trigger. The number of dead channels in the detector is smaller in 2015 than in 2011 and there were other improvements in the detector so one expects a better efficiency and acceptance in this case. Furthermore RUN2 was at a higher energy and the cross section for coherent J/ψ production is expected to grow by a factor 1.6. So one would expect around 50 to 80 events of this type in the currently existing data.

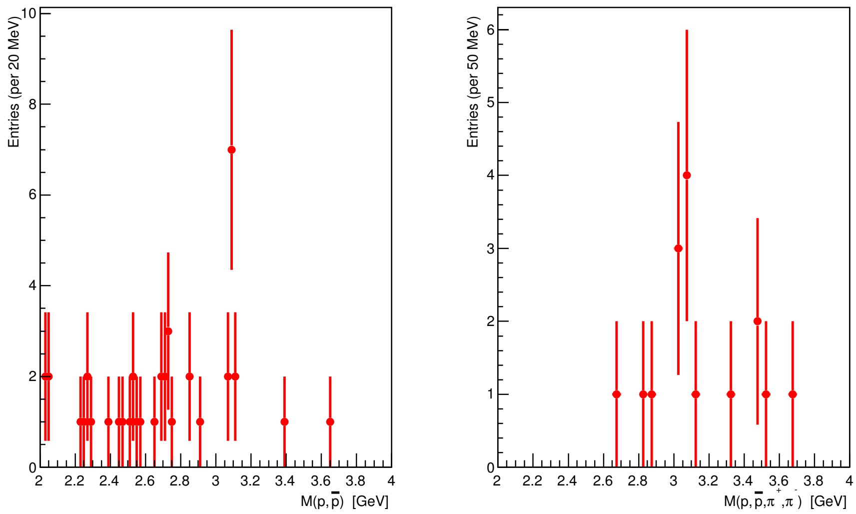

Figure 6.23: Preliminary mass distribution for candidates of J/ψ coherent photoproduction using CCUP4 ALICE data from 2011. Left shows the $J/\psi \rightarrow p\bar{p}$ decay channel and right the $J/\psi \rightarrow p\bar{p}\pi\pi$ channel.

Chapter 7

Summary

The aim of this work was to assess the possibilities of measuring the coherently photoproduced J/ψ decaying into $p\bar{p}$ decay channel in Pb–Pb ultra-peripheral collisions at ALICE. This type of decay has never been studied before in ALICE.

The J/ψ meson is presented in the first chapter and the experiments that led to its discovery are briefly described. I described the ultra-peripheral collisions and the photoproduction. I focused on photoproduction of J/ψ in Pb–Pb collisions which are studied in this work. The previous relevant measurements of the J/ψ particle are mentioned, such as ALICE, HERA and Tevatron experiments. One chapter is dedicated to the description of the ALICE detector at LHC and its subdetectors. The emphasis is put on the subdetectors that are used in this particular analysis.

In this analysis the data generated by STARLIGHT Monte Carlo for RUN1 were used. The total 27000 events were generated. After applying a selection criteria 5742 events were selected and written to the ROOT tree. The events for further analysis were selected by the selection criteria for tracks by the used trigger selection.

The efficiency and the acceptance of the detector was computed as 17.5%. I also computed the efficiency and acceptance of the used triggers. The acceptance and efficiency of the SPD trigger was 75.2% and of the TOF trigger only 27.9%. For this low efficiency of the TOF detector I found no explanation.

The kinematic distributions of the J/ψ was studied. The better resolution for the mass and transverse momentum than it was measured before has been obtained as it was expected. The corresponding distributions can be seen in Figures 6.22, 6.11. Also kinematics of the $p\bar{p}$ tracks were studied.

The last section of the thesis is dedicated to estimation of number of candidates for RUN2. In the Table 6.1 the cross sections for different steps of the selection done in this analysis are summarised. For the RUN1 was expected to find 9 J/$\psi \to p\bar{p}$ candidates and 11 candidates were found in the UPC group of ALICE in this decay channel. Furthermore RUN2 was at higher energy and the cross section for coherently produced J/ψ is expected to grow so it is expected to find around 50 to 80 events of this type in the current data.

Bibliography

[1] E. D. Bloom, D. H. Coward, H. DeStaebler, J. Drees, G. Miller, L. W. Mo, R. E. Taylor, M. Breidenbach, J. I. Friedman, G. C. Hartmann, and H. W. Kendall, *High-energy inelastic $e-p$ scattering at 6° and 10°*, *Phys. Rev. Lett.* **23** (Oct, 1969) 930–934.

[2] S. L. Glashow, J. Iliopoulos, and L. Maiani, *Weak interactions with lepton-hadron symmetry*, *Phys. Rev. D* **2** (Oct, 1970) 1285–1292.

[3] J. E. Augustin, A. M. Boyarski, M. Breidenbach, F. Bulos, J. T. Dakin, G. J. Feldman, G. E. Fischer, D. Fryberger, G. Hanson, B. Jean-Marie, R. R. Larsen, V. Lüth, H. L. Lynch, D. Lyon, C. C. Morehouse, J. M. Paterson, M. L. Perl, B. Richter, P. Rapidis, R. F. Schwitters, W. M. Tanenbaum, F. Vannucci, G. S. Abrams, D. Briggs, W. Chinowsky, C. E. Friedberg, G. Goldhaber, R. J. Hollebeek, J. A. Kadyk, B. Lulu, F. Pierre, G. H. Trilling, J. S. Whitaker, J. Wiss, and J. E. Zipse, *Discovery of a narrow resonance in e^+e^- annihilation*, *Phys. Rev. Lett.* **33** (Dec, 1974) 1406–1408.

[4] J. J. Aubert, U. Becker, P. J. Biggs, J. Burger, M. Chen, G. Everhart, P. Goldhagen, J. Leong, T. McCorriston, T. G. Rhoades, M. Rohde, S. C. C. Ting, S. L. Wu, and Y. Y. Lee, *Experimental observation of a heavy particle j*, *Phys. Rev. Lett.* **33** (Dec, 1974) 1404–1406.

[5] A. J. Baltz, *The Physics of Ultraperipheral Collisions at the LHC*, *Phys. Rept.* **458** (2008) 1–171, [arXiv:0706.3356].

[6] C. A. Bertulani, S. R. Klein, and J. Nystrand, *Physics of ultra-peripheral nuclear collisions*, *Ann. Rev. Nucl. Part. Sci.* **55** (2005) 271–310, [nucl-ex/0502005].

[7] J. G. Contreras and J. D. Tapia Takaki, *Ultra-peripheral heavy-ion collisions at the LHC*, *Int. J. Mod. Phys.* **A30** (2015) 1542012.

[8] S. R. Klein and J. Nystrand, *Exclusive vector meson production in relativistic heavy ion collisions*, *Phys. Rev. C* **60** (Jun, 1999) 014903.

[9] **ALICE** Collaboration, E. Abbas et al., *Charmonium and e^+e^- pair photoproduction at mid-rapidity in ultra-peripheral Pb-Pb collisions at $\sqrt{s_{\mathrm{NN}}}$=2.76 TeV*, *Eur. Phys. J.* **C73** (2013), no. 11 2617, [arXiv:1305.1467].

[10] **H1** Collaboration, A. Aktas et al., *Elastic J/psi production at HERA*, *Eur. Phys. J.* **C46** (2006) 585–603, [hep-ex/0510016].

[11] **ZEUS** Collaboration, S. Chekanov et al., *Exclusive photoproduction of J / psi mesons at HERA*, *Eur. Phys. J.* **C24** (2002) 345–360, [hep-ex/0201043].

[12] **CDF** Collaboration, T. Aaltonen et al., *Observation of exclusive charmonium production and $\gamma + \gamma$ to $\mu^+\mu^-$ in $p\bar{p}$ collisions at $\sqrt{s} = 1.96$ TeV*, *Phys. Rev. Lett.* **102** (2009) 242001, [`arXiv:0902.1271`].

[13] **LHCb** Collaboration, R. Aaij et al., *Exclusive J/ψ and ψ(2S) production in pp collisions at $\sqrt{s} = 7$ TeV*, *J. Phys.* **G40** (2013) 045001, [`arXiv:1301.7084`].

[14] **ALICE** Collaboration, K. Aamodt et al., *The ALICE experiment at the CERN LHC*, *JINST* **3** (2008) S08002.

[15] **ALICE** Collaboration, B. B. Abelev et al., *Performance of the ALICE Experiment at the CERN LHC*, *Int. J. Mod. Phys.* **A29** (2014) 1430044, [`arXiv:1402.4476`].